NASA Technical Paper 3574

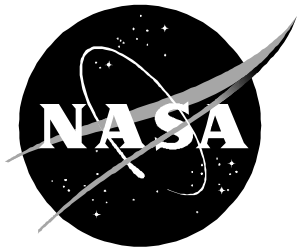

Computational Methods for Frictional Contact With Applications to the Space Shuttle Orbiter Nose-Gear Tire

Development of Frictional Contact Algorithm

John A. Tanner
Langley Research Center • Hampton, Virginia

National Aeronautics and Space Administration
Langley Research Center • Hampton, Virginia 23681-0001

April 1996

Acknowledgment

This report is based on a dissertation submitted to the faculty of the school of Engineering and Applied Sciences of The George Washington University in partial satisfaction of the requirements for the degree of Doctor of Science.

Available electronically at the following URL address: http://techreports.larc.nasa.gov/ltrs/ltrs.html

Printed copies available from the following:

NASA Center for AeroSpace Information
800 Elkridge Landing Road
Linthicum Heights, MD 21090-2934
(301) 621-0390

National Technical Information Service (NTIS)
5285 Port Royal Road
Springfield, VA 22161-2171
(703) 487-4650

Contents

Abstract

A computational procedure is presented for the solution of frictional contact problems for aircraft tires. A Space Shuttle nose-gear tire is modeled using a two-dimensional laminated anisotropic shell theory which includes the effects of variations in material and geometric parameters, transverse-shear deformation, and geometric nonlinearities. Contact conditions are incorporated into the formulation by using a perturbed Lagrangian approach with the fundamental unknowns consisting of the stress resultants, the generalized displacements, and the Lagrange multipliers associated with both contact and friction conditions. The contact-friction algorithm is based on a modified Coulomb friction law. A modified two-field, mixed-variational principle is used to obtain elemental arrays. This modification consists of augmenting the functional of that principle by two terms: the Lagrange multiplier vector associated with normal and tangential node contact-load intensities and a regularization term that is quadratic in the Lagrange multiplier vector. These capabilities and computational features are incorporated into an in-house computer code. Experimental measurements were taken to define the response of the Space Shuttle nose-gear tire to inflation-pressure loads and to inflation-pressure loads combined with normal static loads against a rigid flat plate. These experimental results describe the meridional growth of the tire cross section caused by inflation loading, the static load-deflection characteristics of the tire, the geometry of the tire footprint under static loading conditions, and the normal and tangential load-intensity distributions in the tire footprint for the various static vertical loading conditions. Numerical results were obtained for the Space Shuttle nose-gear tire subjected to inflation pressure loads and combined inflation pressure and contact loads against a rigid flat plate. The experimental measurements and the numerical results are compared.

Introduction

Contact-friction problems are inherently nonlinear and path dependent. Nonlinearity occurs partly because both the contact area and the contact-load intensities are not known beforehand and vary during the loading history. Path dependency is a result of the nonconservative (irreversible dissipative) character of the frictional forces.

A review of static contact problems presented in reference 1, which includes a bibliography of approximately 700 papers, points out that contact problems are important to thermomechanical stress analyses, fracture mechanics, mechanical problems involving elastic foundations, the mechanics of joints, geomechanics, and tires.

Contact problems occupy a position of special importance in aircraft tire mechanics because the contact zone is where the forces are generated that support, guide, and maneuver the airplane. Distributions of contact loads and frictional forces define the moments and shears that are applied to the landing gear system (ref. 2). Under rolling conditions, the distribution of sliding velocities within the tire footprint combined with the frictional forces developed by the tire defines the rate of energy dissipation associated with the loading conditions and provides a measure of tire wear (refs. 3 and 4). In the case of the Space Shuttle orbiter, this wear mechanism is strong enough to cause tire failures during individual landing operations (refs. 5 and 6). Therefore, an understanding of these tire friction forces and the resulting slip velocities is critical to the design of aircraft tires for the next generation of high-performance aircraft, such as the National Aero-Space Plane and the High-Speed Civil Transport.

Modeling contact phenomena in the tire footprint is a formidable task partly because of difficulty of modeling tire response. Distribution of tractions and the footprint geometry are both functions of normal, frictional, and inflation tire loads. Moreover, the complex mechanisms of dynamic friction, which allow the tire to develop the necessary steering and braking forces for aircraft control during ground operations, are not fully understood (ref. 7). The tire analyst thus is forced to choose among several friction theories. When the tire contact problem includes frictional effects, the solution becomes path dependent and a unique solution is not guaranteed.

The aircraft tire is a composite structure of rubber and textile constituents that exhibit anisotropic and nonhomogeneous material properties. Normal tire operating conditions create loads that can produce large deformations. Elevated operating temperatures from the combined effects of material hysteresis and frictional heating can cause variations in the material characteristics of the

tire constituents (refs. 8–10). The laminated carcass of the aircraft tire is thick enough to allow significant transverse-shear deformations.

These facts and attendant difficulties emphasize the need to develop modeling strategies and analysis methods that include efficient, powerful and economic contact algorithms. Intense research has recently focused on nonlinear analyses of static and dynamic problems involving contact. Novel techniques that have emerged from these efforts include semianalytic finite-element models for nonlinear analysis of shells of revolution (refs. 11 and 12), reduced methods (refs. 13 and 14), and operator splitting techniques (refs. 15–17). References 14, 17, and 18 summarize applications of these new tire modeling techniques.

Objectives and Scope

NASA Langley Research Center tire modeling research concentrates on developing an accurate and efficient strategy for predicting aircraft tire responses to a variety of loading conditions. This research focuses on developing tire contact modeling techniques, and the specific objectives of this research are (1) to develop a contact algorithm with friction effects included to predict tire response to combined inflation-pressure and static vertical-loading conditions, (2) to demonstrate the capabilities of this algorithm through numerical studies, and (3) to validate these numerical results with experimental data. Distribution of normal and frictional forces in the tire contact zone (or footprint area) is of particular interest.

The contact algorithm is incorporated into a mixed-formulation, two-field, two-dimensional finite-element model based on the moderate-rotation Sanders-Budiansky shell theory, including the effects of transverse-shear deformations, laminated anisotropic material response, and nonhomogeneous shell characteristics (refs. 19 and 20). A perturbed Lagrangian formulation (refs. 21 and 22) is the basis for this contact algorithm. The Lagrangian formulation uses the preconditioned conjugate gradient (PCG) iteration procedure (refs. 23–25) to determine contact area, distribution of normal force intensities, and allocation of friction force intensities. A modified version of the Coulomb friction law is incorporated into the contact algorithm in which the friction coefficient at the onset of sliding differs from that during sliding. This algorithm also monitors the energy dissipated within the sliding portion of the contact zone. In this investigation it will be assumed that the tire is loaded on a surface that is much stiffer than the tire, thus the surface will be treated as rigid. Hence, the static tire contact problem will be treated as a unilateral contact problem. Reference 26 summarizes the characteristics of this algorithm.

Numerical studies presented for an inflated Space Shuttle nose-gear tire under static load on a flat surface demonstrate the capabilities of the analysis techniques. These analyses incorporate both friction and frictionless contact. Detailed studies are made of the effects of tire tread pattern on the contact-force intensities, the influence of friction coefficient variations on the distribution of tire contact-force intensities, the convergence characteristics of the contact algorithm, and the history of energy dissipation in the static footprint.

Experimental measurements were carried out on the Space Shuttle orbiter nose-gear tire to define its response to combined inflation-pressure and static vertical-loading conditions. Experimental procedures used to define the tire structural response to loading conditions and to measure the footprint-force intensities, and empirical procedures used to define the geometry and construction details of the tire for modeling purposes are discussed. Finally, the analytical results are compared with the experimental measurements.

Reference 27 describes numerical studies, experimental measurements, and comparisons between analytical results and experimental measurements. This report describes development of this contact algorithm.

Nomenclature

A_{ct}	nodal contact area with variable weighting function (see eq. (20))
A_{node}	nodal contact area (see eq. (19))
A_{quad}	area of finite-element quadrant (see eq. (18) and fig. 4)
$a_{11}, a_{22}, a_{12}, a_{ss}, a_{\theta\theta}, a_{s\theta}, b_{11}, b_{22}, b_{12}, g_{11}, g_{22}, g_{12}$	shell compliance coefficients (see eq. (4))
c	number of nodal points in contact within element
c_σ, c_u	portions of shell boundary where tractions and displacements are prescribed
c_{ij}, d_{ij}, f_{ij}	tire stiffness coefficients ($i, j = 1, 2, 6$)
c_{44}, c_{45}, c_{55}	transverse-shear stiffness coefficients of tire (see eq. (A10))

$\hat{e}_s$, $\hat{e}_\theta$	tangential unit vectors in meridional and circumferential directions
$[F]$	flexibility matrix for an individual element
$\{\tilde{f}(Z, p)\}$	vector defined in equation (11)
$\{G(X)\}$	vector of nonlinear terms (see eq. (7))
$\{\bar{G}(X)\}$	vector of nonlinear terms (see eqs. (8) and (9))
$\{\tilde{G}(X)\}$	vector of nonlinear contributions to the global equations (see eqs. (11))
$\bar{g}_u$, $\bar{g}_v$, $\bar{g}_w$	current gaps
$\bar{g}_{u_0}$, $\bar{g}_{v_0}$, $\bar{g}_{w_0}$	initial gaps
$\{g_0\}$	vector of initial gaps for contact element
$\{H\}$	vector of stress-resultant parameters
h	total thickness of tire
$\bar{h}$	nondimensional thickness of tire (see fig. 4)
$[\tilde{K}]$	global linear stiffness matrix (see eq. (11))
M_s, M_θ, $M_{s\theta}$	bending and twisting stress resultants (see fig. 1)
$\{M(H, X)\}$	vector of nonlinear terms (see eq. (7))
m	number of displacement nodes in element
N	shape functions used for approximating generalized displacements and Lagrange multipliers
N_s, N_θ, $N_{s\theta}$	extensional stress resultants
n	total number of degrees of freedom
n_{ct}	peripheral node degrees of freedom (see eq. (20))
n_s, n_θ	unit normal to reference surface
P_n, P_u, P_v	nodal (contact) force
p	load parameter
$\{p\}$	normalized external load parameter
$\{\tilde{P}\}$	global vector of normalized external loads and initial gaps
p_0	intensity of inflation pressure
p_s, p_θ, p	intensity of external loading in coordinate directions (see fig. 1)
$[Q]$, $[R]$	elemental matrices associated with contact condition and regularization term in functional
Q_s, Q_θ	transverse-shear stress resultants (see fig. 1)
R_1, R_2	principal radii of curvature in meridional and circumferential directions
r	normal distance from tire axis to reference surface
$[S]$	strain-displacement matrix for an individual element
s	meridional coordinate of tire (see fig. 1)
$[T]$	transformation matrix
T_n	intensity of contact force acting normal to contact surface
T_r	resultant contact friction force (see eq. (2a))
T_u, T_v	intensity of contact friction forces tangent to contact surface
U	strain energy density (strain energy per unit area)
U_{slip_u}, U_{slip_v}	energy dissipated during slip at each iteration (see eqs. (27))
$\bar{U}_{\text{slip}_u}$, $\bar{U}_{\text{slip}_v}$	energy dissipated during slip over all iterations in a load step (see eqs. (28))
u, v, w	displacement components of reference surface of tire in meridional, circumferential, and normal directions (see fig. 1)
u_{slip}, v_{slip}	tangential slip for each iteration (see eqs. (25))
$\bar{u}_{\text{slip}}$, $\bar{v}_{\text{slip}}$	total tangential slip for each load step (see eqs. (26))
W	external work
$\{X\}$	vector of nodal displacements in shell coordinate system
$\{\bar{X}\}$	vector of nodal displacements in Cartesian coordinate system
x, y, z	Cartesian coordinate system
x_3	coordinate normal to tire reference surface (see fig. 1)
$\{Z\}$	global response vector
$\Delta\bar{g}_u$, $\Delta\bar{g}_v$	slip distances in tire footprint
ε_t, ε_n	penalty parameters in tangential and normal directions (see eq. (6))
$\varepsilon_{\text{relax}}$	relaxation parameter (see eqs. (16))
ε_s, ε_θ, $2\varepsilon_{s\theta}$	extensional strains of reference surface of tire

$2\varepsilon_{s3}$, $2\varepsilon_{\theta 3}$	transverse shear strains of tire
θ	circumferential (hoop) coordinate of tire (see fig. 1)
κ_s, κ_θ, $2\kappa_{s\theta}$	bending strains of tire
$\bar{\lambda}_w$	Lagrange multiplier, representing intensity of contact load normal to contact surface
$\bar{\lambda}_u$, $\bar{\lambda}_v$	Lagrange multipliers, representing intensity of contact friction loads tangent to contact surface
$\bar{\lambda}_{u,\,\mathrm{slip}}$, $\bar{\lambda}_{v,\,\mathrm{slip}}$	Lagrange multipliers, representing sliding friction load intensities
$\{\lambda\}$	vector of nodal values of Lagrange multipliers
μ_{static}	static coefficient of friction
μ_{dynamic}	dynamic coefficient of friction
ξ, η	dimensionless coordinates along meridian (see fig. 4)
Π, $\overline{\Pi}$, Π_{HR}	functionals
ϕ	rotation about normal to tire reference surface (see eq. (A9))
ϕ_s, ϕ_θ	rotational components of reference surface of tire (see fig. 1)
$\Omega^{(e)}$	element domain
Ω_c	contact surface
ψ	angle defined by ratio of two friction forces (see eq. (2d))
∂_s	$\equiv \partial/\partial s$
∂_θ	$\equiv \partial/\partial\theta$
δ	first variation
Superscripts:	
(e)	individual elements
i, j	indices of shape functions for approximating Lagrange multipliers
i'	index of shape function for approximating generalized displacements ($i' = 1, m$)
r	number of iteration cycles
t	matrix transposition

Mathematical Formulation

The analytical formulation for contact of aircraft tires is based on a form of moderate-rotation Sanders-Budiansky shell theory and includes the effects of large displacements and transverse-shear deformation. A mixed formulation is used in which the fundamental unknowns consist of five generalized displacements and eight stress resultants. Figure 1(a) gives sign convention for the generalized displacements and stress resultants and figure 1(b) shows a free body diagram of applied loads, torques, and contact forces. Fundamental equations of the shell theory used herein are given in references 19 and 20 and are summarized in appendix A.

Normal Contact Force Formulation

Figure 2 shows the geometry of contact of a shell pressed against a flat surface. Figure 2(a) shows schematically normal gaps between the tire carcass and the flat surface. In the figure, Ω_c refers to the contact region; $\bar{g}_{w_0}$ is the initial normal gap between the tire shell and the plate; $\bar{g}_w$ is the current normal gap; and T_n is the normal traction on Ω_c. Both $\bar{g}_{w_0}$ and $\bar{g}_w$ are defined to be in the direction of the normal to Ω_c and are measured relative to the inflated profile of the tire. Tire constraints normal to the contact surface can be expressed in terms of the following inequalities and equation that must be satisfied at each point on the contact surface Ω_c:

$$\bar{g}_w \geq 0 \tag{1a}$$

$$T_n \leq 0 \tag{1b}$$

$$T_n \bar{g}_w = 0 \tag{1c}$$

The first inequality (eq. (1a)) represents the kinematic condition of no penetration of the contact surface ($\bar{g}_w = 0$ for the points in contact). The second inequality (eq. (1b)) is the static condition of compressive (or zero) normal tractions. The third equation (eq. (1c)) states that there is zero work done by the normal contact stresses (i. e., the normal contact stresses exist only at the points where the tire is in contact with the rigid plate). The following inequalities are henceforth referred to as the *inactive contact conditions*:

$$\bar{g}_w > 0 \tag{1d}$$

$$T_n > 0 \tag{1e}$$

Equations (1) must be satisfied for both frictionless and frictional contact.

Tangential Contact Force Formulation

Equations (1) define the normal tire contact constraint conditions and are augmented to include friction constraints associated with the Coulomb friction law when friction forces are considered. The Coulomb friction law is modified to include a static friction coefficient associated with the nonskidding or “stick” friction constraint, and a dynamic friction coefficient associated with

the slip condition when the static friction constraint is violated.

The "stick" condition defining the static friction constraint is

$$\sqrt{(T_u^2 + T_v^2)} / T_n \le \mu_{\text{static}} \tag{2a}$$

$$T_u = \cos(\psi) T_n \mu_{\text{dynamic}} \tag{2b}$$

$$T_v = \sin(\psi) T_n \mu_{\text{dynamic}} \tag{2c}$$

represent the slip condition when equation (2a) is violated, where T_u and T_v are the tangential tractions on the friction surface representing the friction forces. The angle ψ defines the ratio between the two friction force components for the slip condition and is expressed as:

$$\psi = \text{abs}\left[\arctan\left(\frac{T_v}{T_u}\right)\right] \tag{2d}$$

where T_u and T_v in equation (2d) are the computed tangential traction components that exist whenever the static friction constraint in equation (2a) is first violated. The following inequalities also hold on the friction surface:

$$\mu_{\text{dynamic}} \le \mu_{\text{static}} \tag{2e}$$

$$T_u \Delta \bar{g}_u \le 0 \tag{2f}$$

$$T_v \Delta \bar{g}_v \le 0 \tag{2g}$$

Inequality (2e) simply states that the dynamic friction coefficient cannot be greater than the static friction coefficient. Inequalities (2f) and (2g) state that the energy dissipated by sliding is never positive since the friction forces always oppose slipping in the tire footprint.

Figure 2(b) shows schematically the relationship among the various tangential gap definitions. Initial gaps $\bar{g}_{u_0}$ and $\bar{g}_{v_0}$ represent the tangential displacement of the inflated tire from the uninflated configuration. Current gaps $\bar{g}_u$ and $\bar{g}_v$ represent the displacement of the current contact solution from the inflated configuration. Delta gaps $\Delta\bar{g}_u$ and $\Delta\bar{g}_v$ represent the tangential slip distances from the previous tire contact "stick" location in the tire footprint. For nodes not currently in contact with the flat plate, the initial gaps and current gaps represent the orthogonal projections of the gap expressions on the contact surface. Delta gaps are defined only after contact has been established.

Governing Finite-Element Equations

Discrete equations governing the response of the tire are obtained by applying a modified form of the two-field, Hellinger-Reissner mixed-variational principle. This principle can be expressed in the following form:

$$\delta\Pi_{HR}(N_s, N_\theta, N_{s\theta}, M_s, M_\theta, M_{s\theta}, Q_s, Q_\theta, u, v, w, \phi_s, \phi_\theta) = \delta\overline{\Pi} - \delta W \tag{3}$$

where

$$\begin{aligned}
\overline{\Pi} = \int_\Omega \Bigg\{ & N_s\left[\partial_s u + \frac{w}{R_1} + \frac{1}{2}\left(\frac{u}{R_1} - \partial_s w\right)^2 + \frac{1}{2}\phi^2\right] + N_\theta\left[\frac{\partial_s r}{r}u + \frac{1}{r}\partial_\theta v + \frac{w}{R_2} + \frac{1}{2}\left(\frac{v}{R_2} - \frac{1}{r}\partial_\theta w\right)^2 + \frac{1}{2}\phi^2\right] \\
& + N_{s\theta}\left[\frac{1}{r}\partial_\theta u + \left(\partial_s - \frac{\partial_s r}{r}\right)v + \left(\frac{u}{R_1} - \partial_s w\right)\left(\frac{v}{R_2} - \frac{1}{r}\partial_\theta w\right)\right] + M_s \partial_s \phi_s + M_\theta\left(\frac{\partial_s r}{r}\phi_s + \frac{1}{r}\partial_\theta \phi_\theta\right) \\
& + M_{s\theta}\left[\frac{1}{r}\partial_\theta \phi_s + \left(\partial_s - \frac{\partial_s r}{r}\right)\phi_\theta + \left(\frac{1}{R_1} - \frac{1}{R_2}\right)\phi\right] + Q_s\left(-\frac{u}{R_1} + \partial_s w + \phi_s\right) + Q_\theta\left(-\frac{v}{R_2} + \frac{1}{r}\partial_\theta w + \phi_\theta\right) \\
& - \Bigg[\frac{1}{2}(a_{11}N_s^2 + a_{22}N_\theta^2 + g_{11}M_s^2 + g_{22}M_\theta^2 + a_{ss}Q_s^2 + a_{\theta\theta}Q_\theta^2) + a_{12}N_s N_\theta + b_{11}N_s M_s + b_{12}N_s M_\theta \\
& + b_{12}N_\theta M_s + b_{22}N_\theta M_\theta + g_{12}M_s M_\theta + a_{s\theta}Q_s Q_\theta\Bigg]\Bigg\} d\Omega
\end{aligned} \tag{4}$$

and

$$W = \int_{\Omega} (p_s u + p_\theta v + p w)\, d\Omega + \int_{c_\sigma} \Bigg(\Bigg\{ \tilde{N}_s u + \tilde{N}_{s\theta} v + \tilde{M}_s \phi_s + \tilde{M}_{s\theta} \phi_\theta + \underline{\Bigg[\tilde{Q}_s + \tilde{N}_s \left(\frac{u}{R_1} - \partial_s w \right) + \tilde{N}_{s\theta} \left(\frac{v}{R_2} - \frac{1}{r} \partial_\theta w \right) \Bigg] w} \Bigg\} n_s$$

$$+ \Bigg\{ \tilde{N}_{s\theta} u + \tilde{N}_\theta v + \tilde{M}_{s\theta} \phi_s + \tilde{M}_\theta \phi_\theta + \underline{\Bigg[\tilde{Q}_\theta + \tilde{N}_{s\theta} \left(\frac{u}{R_1} - \partial_s w \right) + \tilde{N}_\theta \left(\frac{v}{R_2} - \frac{1}{r} \partial_\theta w \right) \Bigg] w} \Bigg\} n_\theta \Bigg)\, dc$$

$$+ \int_{c_u} \Bigg(\Bigg\{ \tilde{N}_s (-\tilde{u} + u) + \tilde{N}_{s\theta} (-\tilde{v} + v) + \tilde{M}_s (-\tilde{\phi}_s + \phi_s) + \tilde{M}_{s\theta} (-\tilde{\phi}_\theta + \phi_\theta) + \underline{\Bigg[\tilde{Q}_s + \tilde{N}_s \left(\frac{u}{R_1} - \partial_s w \right) + \tilde{N}_{s\theta} \left(\frac{v}{R_2} - \frac{1}{r} \partial_\theta w \right) \Bigg]}$$

$$\times (-\tilde{w} + w) \Bigg\} n_s + \Bigg\{ \tilde{N}_{s\theta} (-\tilde{u} + u) + \tilde{N}_\theta (-\tilde{v} + v) + \tilde{M}_{s\theta} (-\tilde{\phi}_s + \phi_s) + \tilde{M}_\theta (-\tilde{\phi}_\theta + \phi_\theta)$$

$$+ \underline{\Bigg[\tilde{Q}_\theta + \tilde{N}_{s\theta} \left(\frac{u}{R_1} - \partial_s w \right) + \tilde{N}_\theta \left(\frac{v}{R_2} - \frac{1}{r} \partial_\theta w \right) \Bigg] (-\tilde{w} + w)} \Bigg\} n_\theta \Bigg)\, dc \tag{5}$$

In equations (4) and (5), a, b, and g are shell compliance coefficients which are the inverse of the shell stiffness coefficients given in appendix A; ϕ is the rotation about the normal to the shell and is also given in appendix A; p_s, p_θ, and p are the intensities of the external distributed loads in the meridional, circumferential, and radial directions, respectively; Ω is the shell domain; and c_σ and c_u are the portions of the boundary over which tractions and displacements are prescribed. Quantities with a tilde (~) denote prescribed boundary stress resultants and generalized displacements; the underlined terms in equations (4) and (5) represent nonlinear contributions; and n_s and n_θ are unit normals to the boundary.

Modification to the variational principle consists of augmenting the functional of that principle by two terms: the Lagrange multiplier associated with the nodal contact pressures and a regularization term which is quadratic in the Lagrange multipliers. References 21, 22, and 28 give a detailed discussion of the perturbed and the augmented Lagrangian formulations.

The modified functional has the following form:

$$\Pi = \Pi_{HR} + \int_{\Omega_c} \left[\bar{\lambda} \bar{g} - \frac{1}{2\varepsilon} (\bar{\lambda})^2 \right] d\Omega \tag{6}$$

where Π_{HR} is the functional of the Hellinger-Reissner variational principle; $\bar{\lambda}$ is the Lagrange multiplier; and ε is the penalty parameter associated with the regularization term. Note that the addition of the regularization term amounts to approximating the rigid plate by continuously distributed springs with stiffness of ε, for sufficiently large ε. As $1/\varepsilon$ approaches zero, the continuous springs become the rigid plate.

Shape functions used in approximating the generalized displacements and the Lagrange multipliers are selected to be the same and differ from those used in approximating the stress resultants. Moreover, because of the nature of the functional Π in equation (6), the continuity of neither the stress resultants nor the Lagrange multiplier is imposed at the interelement boundaries.

Finite-element equations for each individual element can be cast in the following compact form:

$$\begin{bmatrix} -F & S & \bullet \\ S^t & \bullet & Q \\ \bullet & Q^t & \dfrac{R}{\varepsilon} \end{bmatrix}^{(e)} \begin{Bmatrix} H \\ X \\ \lambda \end{Bmatrix}^{(e)} + \begin{Bmatrix} G(X) \\ M(H, X) \\ \bullet \end{Bmatrix}^{(e)} - \begin{Bmatrix} \bullet \\ pP \\ g_0 \end{Bmatrix}^{(e)} = 0 \tag{7}$$

where $\{H\}$, $\{X\}$, and $\{\lambda\}$ are the vectors of the stress-resultant parameters, nodal values of the generalized displacements, and nodal values of the Lagrange multipliers, respectively, $[F]$ is the matrix of linear flexibility coefficients, $[S]$ is the strain-displacement matrix, $[Q]$ and $[R]$ are the matrices associated with the contact condition and the regularization term in the functional, respectively, $\{G(X)\}$ and $\{M(H, X)\}$ are vectors of nonlinear terms, and $\{g_0\}$ is the vector of initial gaps in the contact region Ω_c. A dot refers to a zero submatrix or subvector, superscript (e) refers to individual elements, $\{P\}$ is the normalized external load vector, and p is a load parameter. As the load is incremented, only the value of the load parameter p changes and the normalized load vector $\{P\}$ is constant. Appendix B gives the formulas for the elemental arrays $[F]$, $[S]$, $\{G(X)\}$, $\{M(H, X)\}$, $[Q]$, $[R]$, $\{P\}$, and $\{g_0\}$.

Note that the sizes of the coefficient matrices $[Q]$, $[R]$, and $\{g_0\}$ vary with the number of active contact conditions. The difficulty associated with an equation system whose size varies during the solution process is alleviated by allowing the Lagrange multipliers to be discontinuous at interelement boundaries and then eliminating them on the element level. If the stress-resultant parameters and Lagrange multiplier parameters are eliminated from equation (7) then the following equations in terms of nodal displacements $\{X\}$ are obtained:

$$\left[[S]^t[F]^{-1}[S] - \varepsilon[Q][R]^{-1}[Q]^t\right]^{(e)}\{X\}^{(e)} + \{\bar{G}(X)\}^{(e)} + \varepsilon[Q][R]^{-1}\{g_0\}^{(e)} - p\{P\}^{(e)} = 0 \tag{8}$$

where

$$\{\bar{G}(X)\}^{(e)} = [S]^t[F]^{-1}\{G(X)\}^{(e)} + \{M(H, X)\}^{(e)} \tag{9}$$

and the vector $\{H\}$ in $\{M(H, X)\}$ is replaced by its expression in terms of $\{X\}$. Equation (8) is the tangent operator for the Newton-Raphson iterative solution procedure used in this investigation and is derived in detail in appendix C.

To simplify the treatment of the contact conditions, the displacement components are transformed from shell coordinates (s, θ, x_3) to the global Cartesian coordinates (x, y, z) before assembly. The relations between the displacement vector in the shell coordinates $\{X\}^{(e)}$ and the corresponding vector in Cartesian coordinates $\{\bar{X}\}^{(e)}$ can be written in the following compact form:

$$\{X\}^{(e)} = [T]\{\bar{X}\}^{(e)} \tag{10}$$

where $[T]$ is the transformation matrix. The different arrays in the finite-element equations are transformed accordingly. Appendix D gives the explicit form of the transformation relations.

Solution of Nonlinear Algebraic Equations

Discrete equations governing the response of the tire are obtained by assembling the elemental contributions in equation (6) or (7) and can be written in the following form:

$$\{\tilde{f}(Z, p)\} = [\tilde{K}]\{Z\} + \{\tilde{G}(Z)\} - p\{\tilde{P}\} = 0 \tag{11}$$

where $[\tilde{K}]$ is the global linear stiffness matrix of the tire; $\{\tilde{G}(Z)\}$ is the vector of nonlinear contributions; $\{\tilde{P}\}$ is the global vector of normalized external loads and initial gaps; and $\{Z\}$ is the global response vector of the tire obtained by assembling the contributions from the subvectors $\{H\}$, $\{X\}$, and $\{\lambda\}$.

The nonlinear algebraic equation (eq. (8)) is solved and the contact region and the contact-load intensities are determined by using an incremental-iterative technique (i.e., a predictor-corrector computation method) in which the response vector $\{Z\}$, corresponding to a particular value of the load parameter p, is used to calculate a suitable approximation (predictor) for $\{Z\}$ at a different value of p. This approximation is then chosen as an initial estimate for $\{Z\}$ in a corrective iterative scheme such as the Newton-Raphson technique. In each Newton-Raphson iteration the contact conditions are checked and updated.

Computational Procedures to Determine Contact-Load Intensities, Contact Areas, and Energy Dissipated During Slip

This section describes the contact algorithm used to assess the state of contact in the tire footprint and to implement the modified Coulomb friction law. Descriptions of the algorithms used to approximate the area of contact and the energy dissipated during slip are also included. Finally, the computational procedures used to determine the displacement, stress-resultant, and contact-load intensity solutions at each iteration and load step are outlined.

Nonlinearities due to large displacements (moderate rotations) and the contact condition are combined into a

single iteration loop. Reference 23 advocates a two-level (nested) iteration scheme. For this two-level scheme, the inner iteration loop accounts for the contact conditions associated with the contact-load intensities, and the outer iteration loop uses the Newton-Raphson iteration scheme. Numerical experiments demonstrate that for frictionless contact problems the two-level iterative scheme requires more iterations than the single-level scheme utilized in the present study. (See ref. 29.)

Contact Algorithm With Friction

Figure 3 schematically shows the contact algorithm developed for this investigation. Three possible contact states are possible for each contact node in this algorithm: (1) open or no contact, denoted by the contact flag set to 0; (2) stick contact where the contact node adheres to the contact surface, denoted by the contact flag set to 1; and (3) slip contact where the contact node slides on the contact surface, denoted by the contact flag set to 2. The algorithm is built on a two-level logical if-statement scheme. The first level interrogates the status of the previous contact flags for each contact node. The second level interrogates the status of the current normal gap $\bar{g}_w$ of nodes not previously in contact to determine whether or not contact has been established for that particular node; for nodes which were previously in contact, the second level interrogates both the sign of the normal Lagrange multiplier $\bar{\lambda}_w$, which represents the normal contact load intensity, and the Coloumb friction law constraints to determine the current nodal contact status.

For nodes not previously in contact, stick contact is assumed whenever the normal gap $\bar{g}_w$ is positive or 0, i.e., inequality equation (1a) is satisfied, and no contact is assumed whenever $\bar{g}_w$ is negative. For nodes previously in contact, stick contact is assumed if both the static condition of compressive (or 0) normal tractions (eq. (1b)) and the static friction constraint (eq. (2a)) are satisfied; slip contact is assumed if the compressive normal tractions condition is satisfied but the friction constraint is not satisfied at a node. If the compressive normal tractions condition is not satisfied at a node, then that node is removed from the list of active contact nodes.

When an open nodal contact condition is encountered the contact flag is set to 0; if the previous contact condition was either stick or slip then the three load intensities $\{\bar{\lambda}_u, \bar{\lambda}_v, \bar{\lambda}_w\}$ for that node are set to 0. When a stick nodal contact condition is encountered the contact flag is set to 1, the number of boundary condition nodes is incremented, and incremental tangential nodal displacements Δu and Δv are set to 0. When a slip nodal contact condition is encountered the contact flag is set to 2. The dynamic friction-force load intensities are computed from the following equations:

$$\bar{\lambda}_{u,\,\mathrm{slip}} = \cos(\psi)\bar{\lambda}_n\mu_{\mathrm{dynamic}} \tag{12a}$$

$$\bar{\lambda}_{v,\,\mathrm{slip}} = \sin(\psi)\bar{\lambda}_n\mu_{\mathrm{dynamic}} \tag{12b}$$

Incremental friction-force load intensities required to bring the friction-force load intensities back into compliance with the Coulomb friction law constraint are computed from

$$\Delta\bar{\lambda}_u = \bar{\lambda}_{u,\,\mathrm{slip}} - \bar{\lambda}_u \tag{13a}$$

$$\Delta\bar{\lambda}_v = \bar{\lambda}_{v,\,\mathrm{slip}} - \bar{\lambda}_v \tag{13b}$$

The delta gaps associated with the sliding friction condition are computed as follows

$$\Delta\bar{g}_u = \frac{(\{\mathrm{rlbar}\} - \Delta\bar{\lambda}_u)}{\{\mathrm{dlbar}\}} \tag{14a}$$

$$\Delta\bar{g}_v = \frac{(\{\mathrm{rlbar}\} - \Delta\bar{\lambda}_v)}{\{\mathrm{dlbar}\}} \tag{14b}$$

where equations (14) are derived from equation (C44) in appendix C and the delta gaps replace the displacement solution. The vectors {rlbar} and {dlbar} are defined in appendix C. The incremental friction-force load intensities (eqs. (13)) are used to update the contact solution

$$\bar{\lambda}_u^c = \bar{\lambda}_u^c + \Delta\bar{\lambda}_u^c \tag{15a}$$

$$\bar{\lambda}_v^c = \bar{\lambda}_v^c + \Delta\bar{\lambda}_v^c \tag{15b}$$

and the delta gaps (eqs. (14)) are used to update the displacement solution

$$u^c = u^c + \varepsilon_{\mathrm{relax}}\Delta g_u^c \tag{16a}$$

$$v^c = v^c + \varepsilon_{\mathrm{relax}}\Delta g_v^c \tag{16b}$$

where $\varepsilon_{\mathrm{relax}}$ is a relaxation parameter with a magnitude $0 < \varepsilon_{\mathrm{relax}} < 1$. The function of $\varepsilon_{\mathrm{relax}}$ is to enhance the convergence characteristics of the contact algorithm. Index c ranges from 1 to the number of contact nodes.

Determination of Contact Area

To obtain an accurate approximation of the contact area of the Space Shuttle nose-gear tire under static loading conditions, an algorithm was developed which employs information from the initial geometry of the tire footprint and updates this geometry to accommodate footprint deformations associated with contact. Figure 4

illustrates major features of this contact area algorithm. The 9-noded element is conveniently subdivided into four quadrants with a node on the corners of each quadrant. Coordinates of the quadrant corners are defined as

$$x^i = x_0^i + u^i \tag{17a}$$

$$y^i = y_0^i + v^i \tag{17b}$$

where x_0^i and y_0^i are the initial coordinates of the node and u^i and v^i are the tangential nodal displacement components. Index i ranges from 1 to the number of nodes in the element. As figure 4 indicates, the area of a typical quadrant is

$$\begin{aligned} A_{\text{quad}} = 0.5(&x^a y^b - x^b y^a + x^b y^c - x^c y^b + x^c y^a - x^a y^c \\ &+ x^a y^c - x^c y^a + x^c y^d - x^d y^c + x^d y^a - x^a y^d) \end{aligned} \tag{18}$$

where the superscripts a, b, c, and d denote the four corners of the quadrant, starting from the lower left and advancing counterclockwise around the quadrant. Nodal areas associated with contact nodes within a 9-noded element are

$$\left.\begin{aligned} A_{\text{node}}^1 &= 0.25A_{\text{quad}}^1 \\ A_{\text{node}}^2 &= 0.25(A_{\text{quad}}^1 + A_{\text{quad}}^2) \\ A_{\text{node}}^3 &= 0.25A_{\text{quad}}^2 \\ A_{\text{node}}^4 &= 0.25(A_{\text{quad}}^2 + A_{\text{quad}}^3) \\ A_{\text{node}}^5 &= 0.25A_{\text{quad}}^3 \\ A_{\text{node}}^6 &= 0.25(A_{\text{quad}}^3 + A_{\text{quad}}^4) \\ A_{\text{node}}^7 &= 0.25A_{\text{quad}}^4 \\ A_{\text{node}}^8 &= 0.25(A_{\text{quad}}^4 + A_{\text{quad}}^1) \\ A_{\text{node}}^9 &= 0.25(A_{\text{quad}}^1 + A_{\text{quad}}^2 + A_{\text{quad}}^3 + A_{\text{quad}}^4) \end{aligned}\right\} \tag{19}$$

When there is only partial contact within an element, i.e., only some nodes are in contact, then a variable weighting function is used to modify the nodal contact areas as follows:

$$A_{ct}^i = 0.5\left(1.0 + \frac{\sum_{k=1}^{n_{ct}} ct^k}{n_{ct}}\right) A_{\text{node}}^i \tag{20}$$

where A_{ct}^i is the modified contact area associated with a node in contact, and ct^k is defined as

$$ct^k = \begin{cases} 1 \text{ if node}^k \text{ is in contact} \\ 0 \text{ if node}^k \text{ is not in contact} \end{cases} \tag{21}$$

where node^k is a node on the periphery of the quadrant or quadrants defining the nodal areas. For the corner nodes of the 9-noded finite element shown in figure 4, n_{ct} is 3; for the midside nodes n_{ct} is 5; and for the interior node n_{ct} is 8. The peripheral nodes associated with corner node 1 are (2, 8, 9); the peripheral nodes for midside node 2 are (1, 3, 4, 8, 9); and the peripheral nodes for the interior node 9 are (1, 2, 3, 4, 5, 6, 7, 8). Finally, the nodal areas from each element are assembled into a global contact node array so that the nodal areas reflect the contributions from all shared elements.

Special Treatment for Tread Grooves

To facilitate adequate modeling of the 3-circumferential groove tread pattern of the Space Shuttle nose-gear tire, modifications were made to the vector of initial normal gaps $\{\bar{g}_{w_0}\}$ and to the variable weighting function used to define the contact area. For nodes in the region of a tread groove, a positive number was added to $\bar{g}_{w_0}$ to prevent that node from contacting the surface. For this investigation the following modification was made:

$$\bar{g}_{w_0}^g = \bar{g}_{w_0}^g + 3.1 \tag{22}$$

where the superscript ranges over the node numbers associated with tread groove locations. Nodal areas for contact nodes adjacent to the center groove were computed directly from equations (19) and the variable weighting function (eq. (20)) was not used for those nodes. Nodal areas for contact nodes adjacent to either of the remaining tread grooves were computed with the variable weighting function (eq. (20)) modified to reflect fewer peripheral contact nodes. For example, suppose the right edge of the finite element shown in figure 4 coincides with the left edge of a tread groove such that nodes (3, 4, 5) are in the groove and never contact the surface. For this situation n_{ct} for midside nodes (2, 6) is 3, and their peripheral nodes are (1, 8, 9) and (7, 8, 9), respectively. For the interior node (9) n_{ct} is 5, and the peripheral nodes are (1, 2, 6, 7, 8).

Evaluation of Contact Forces From Load Intensities

Solution of the governing discrete equations of the entire structure generates the nodal displacements, the stress-resultant parameters, and the values of the Lagrange multipliers at the contact nodes. For each

individual element in contact, the intensity of the contact-load intensities at a node $\{T_u, T_v, T_n\}$ are equal to the values of the Lagrange multipliers $\{\bar{\lambda}_u, \bar{\lambda}_v, \bar{\lambda}_w\}$ at the same node. Reference 30 states the contact-load intensities may be expressed as a function of the nodal forces $\{P_u^i, P_v^i, P_n^i\}$ as follows:

$$\begin{Bmatrix} P_u^i \\ P_v^i \\ P_n^i \end{Bmatrix} = \int_{\Omega^{(e)}} N^i N^j d\Omega \begin{Bmatrix} T_u^i \\ T_v^j \\ T_n^j \end{Bmatrix} \tag{23}$$

where N^i are the shape functions used in approximating the Lagrange multipliers and the generalized displacements, and $\Omega^{(e)}$ is the domain of the contact element. The indicated numerical integration in equation (23) was implemented with a Newton-Cotes quadrature formulation. The range of both i and j in equation (23) is from 1 to the number of displacement nodes in the element. References 29, 31, and 32 use this method in the analysis of frictionless contact problems. This method of extracting contact forces from the load intensities is consistent with the finite-element formulation of the problem.

A possible drawback of this method is the fact that the shape functions N^i are computed only for the undeformed tire and may not reflect contact area variations associated with tire deformations at the tire-pavement interface. An alternative method of obtaining contact forces from the load intensities that alleviates this drawback is expressed in the following equation:

$$\begin{Bmatrix} P_u^c \\ P_v^c \\ P_n^c \end{Bmatrix} = \begin{Bmatrix} (A_{ct}T_u)^c \\ (A_{ct}T_v)^c \\ (A_{ct}T_n)^c \end{Bmatrix} \tag{24}$$

where c ranges from 1 to the number of contact nodes. Reference 30 discusses other approaches for determining the contact forces.

Evaluation of Energy Dissipated During Slip

For contact problems involving friction it is important to account for any slip that occurs in the contact area. In this investigation the slip at each contact node is approximated for each iteration with the following equations:

$$u_{\text{slip}}^{c(k)} = \Delta g_u^{c(k)} \varepsilon_{\text{relax}} \tag{25a}$$

$$v_{\text{slip}}^{c(k)} = \Delta g_v^{c(k)} \varepsilon_{\text{relax}} \tag{25b}$$

where u_{slip} and v_{slip} represent the tangential slip in the tire meridional and circumferential directions, respectively. Index c ranges from 1 to the number of contact nodes and the index k ranges from 1 to the number of iterations at each load step. For a given contact node, the total slip associated with a load step is

$$\bar{u}_{\text{slip}}^{c} = \sum_{k=1}^{\text{iter}} u_{\text{slip}}^{c(k)} \tag{26a}$$

$$\bar{v}_{\text{slip}}^{c} = \sum_{k=1}^{\text{iter}} v_{\text{slip}}^{c(k)} \tag{26b}$$

The magnitude of these total slip values $\bar{u}_{\text{slip}}^{c}$ and $\bar{v}_{\text{slip}}^{c}$ should increase monotonically over the iterations that involve sliding contact. Energy dissipated through slip was computed at each iteration for each contact node as

$$U_{\text{slip}_u}^{c(k)} = [A_{ct}(u_{\text{slip}}T_u)^{(k)}]^c \tag{27a}$$

$$U_{\text{slip}_v}^{c(k)} = [A_{ct}(v_{\text{slip}}T_v)^{(k)}]^c \tag{27b}$$

where the energy dissipation expressions (U_{slip_u}, U_{slip_v}) should always be negative since the friction forces ($T_u A_{ct}, T_v A_{ct}$) oppose the slip. Energy expressions (eqs. (26)) are summed over the number of iterations to obtain an estimate of the total energy dissipated through sliding at each contact node and load step as follows:

$$\bar{U}_{\text{slip}_u}^{c} = \left[A_{ct} \sum_{k=1}^{\text{iter}} (u_{\text{slip}}T_u)^{(k)}\right]^c \tag{28a}$$

$$\bar{U}_{\text{slip}_v}^{c} = \left[A_{ct} \sum_{k=1}^{\text{iter}} (v_{\text{slip}}T_v)^{(k)}\right]^c \tag{28b}$$

Computational Procedures for Solving Tire Contact Problem

The computational procedure used in the present study is summarized as follows:

Preprocessing and Initial Calculation Phases

Step 1. Model tire geometry, evaluate stiffness coefficients (ref. 31), and generate input data including transformation matrices.

Step 2. Select estimates for the penalty parameters and assume the contact status at the selected contact nodes.

Step 3. Generate linear element arrays.

Solution Phase

Step 4. Solve inflation-pressure case without contact using Newton-Raphson iteration scheme.

Step 5. Generate initial normal gap between the inflated tire configuration and flat surface at designated contact nodes.

- Begin displacement incrementation loop.
- Begin combined contact and Newton-Raphson iteration loop.

Step 6. Generate nonlinear element arrays, eliminate the stress resultants and the Lagrange multipliers from the elemental equations, and assemble the left- and right-hand sides of the equations.

Step 7. Solve equation (8) for the incremental displacements.

Step 8. Update the response vector for displacements, stress resultants, and the Lagrange multipliers:

$$\{Z^{(r+1)}\} = \{Z^{(r)}\} + \{\Delta Z^{(r)}\} \tag{29}$$

Step 9. Check the contact status and modify the contact conditions at each node as needed:

if $\bar{g}_w < 0$ and $\lambda_w < 0$, then the constraint is active

if $\bar{g}_w > 0$ or $\lambda_w > 0$, then the contact constraint is inactive

if $T_r = \sqrt{(T_u^2 + T_v^2)} \le T_n \mu_{\text{static}}$ then the contact condition is stick

if $T_r = \sqrt{(T_u^2 + T_v^2)} > T_n \mu_{\text{static}}$ then the contact condition is slip

When the previous normal contact constraint is inactive, proceed as follows:

a. If the current normal contact constraint is also inactive, then continue.

b. If the current normal contact constraint is active, add the active contact contribution to the list of nodes with stick contact, increment boundary conditions, and continue.

When the previous contact constraint condition is stick or slip, proceed as follows:

a. If the current contact constraint is stick, increment boundary conditions and continue.

b. If the current contact condition is slip, define dynamic friction forces and continue.

c. If the current normal contact constraint is inactive, remove the node from the list of active constraints, zero out contact forces, and continue.

If any current contact constraints are different from the previous constraints or if there are any active slip constraints, return to step 6.

Step 10. Check the convergence of the Newton-Raphson iterations:

$$e = \frac{[\{\Delta Z\}^t \{\Delta Z\} / \{Z\}^t \{Z\}]^{1/2}}{n} < \text{Tolerance} \tag{30}$$

where n is the total number of degrees of freedom in the model and the tolerance is prescribed. If convergence is achieved, then compute the contact forces at each contact node with equation (24) or with the following:

$$\begin{Bmatrix} P_u^i \\ P_v^i \\ P_n^i \end{Bmatrix} = \int_{\Omega^{(e)}} N^i N^j \begin{Bmatrix} \bar{\lambda}_u^j \\ \bar{\lambda}_v^j \\ \bar{\lambda}_n^j \end{Bmatrix} d\Omega \tag{31}$$

and continue. Otherwise return to step 6.

Step 11. If the prescribed displacement is greater than the specified maximum displacement, then stop. Otherwise, add additional displacement and return to step 6.

The mixed-formulation finite elements used in this study have nine displacement nodes and four stress-resultant nodes and are designated as M9-4 elements in table 1.

Comments on Mixed Models, Perturbed Lagrangian Formulation, and Computational Procedure

The following comments regarding the mixed models, the perturbed Lagrangian formulation, and the computational procedure used herein are in order:

1. Nonlinear terms in the finite-element equations of the mixed model (eq. (7)) have a simpler form than those of the corresponding displacement model (eq. (9)).
2. Equation (7) includes both the Lagrange multiplier approach and the penalty method as special cases, as follows:

a. As the penalty parameters ε_n and ε_t approach infinity, equation (7) reduces to those of the Lagrange multiplier approach.

b. When Lagrangian multiplier terms are eliminated in equation (7), the resulting equations are identical to the penalty method.

3. The perturbed Lagrangian formulation alleviates two of the drawbacks associated with the Lagrangian multiplier approach and the penalty method, namely,

   a. The regularization term in the functional results in replacing one of the zero diagonal blocks in the discrete equations of the Lagrangian multiplier approach by the diagonal matrix $[R]/\varepsilon$ in equation (7).

   b. The contact condition is satisfied exactly by transforming the constrained problem to an unconstrained problem through the introduction of Lagrangian multipliers (the terms

$$\int_{\Omega_c} \bar{\lambda}_u \bar{g}_u \, d\Omega, \int_{\Omega_c} \bar{\lambda}_v \bar{g}_v \, d\Omega, \text{ and } \int_{\Omega_c} \bar{\lambda}_w \bar{g}_w \, d\Omega$$

   in equation (6)) rather than approximately as in the penalty method. However, the presence of the regularization terms (the terms

$$-\int_{\Omega_c} \frac{1}{2\varepsilon_t}(\bar{\lambda}_u)^2 \, d\Omega - \int_{\Omega_c} \frac{1}{2\varepsilon_t}(\bar{\lambda}_v)^2 \, d\Omega - \int_{\Omega_c} \frac{1}{2\varepsilon_n}(\bar{\lambda}_w)^2 \, d\Omega$$

   in equation (6)) results in replacing the contact condition by the perturbed condition:

$$\frac{1}{\varepsilon}[R]\{\lambda\} + [Q]^t\{X\} - \{g_0\} = 0 \qquad (32)$$

4. An important consideration in the perturbed Lagrangian formulation and in any penalty formulation is the proper selection of the penalty parameters ε_n and ε_t. With the foregoing mixed models the penalty parameters can be chosen independently of the element size without adversely affecting the performance of the model. Accuracy of the contact solution increases with increasing values of the penalty parameter ε_n. However, for very large values of ε_n, the equations become ill-conditioned and thus round off errors increase. For small values of ε_t the tire footprint becomes compliant, i.e., there is little or no slipping, and the calculated friction forces are artificially low. For very high values of ε_t the contact algorithm with friction may become ill-conditioned.

5. The elemental arrays $[F]$, $[S]$, $\{G(X)\}$, $\{M(H, X)\}$, and $\{P\}$ are evaluated numerically using a Gauss-Legendre formula. The arrays $[Q]$, $[R]$, and $\{g_0\}$ are evaluated using a Newton-Cotes formula. In both cases the number of quadrature points used is the same as the number of displacement nodes in the element. This results in under-integrating the arrays $[Q]$ and $[R]$ and avoids the oscillatory behavior of the contact-load intensity that has been observed when the arrays are fully integrated. Note that the use of Newton-Cotes formula allows the contact-load intensities to be evaluated at the displacement nodes. Appendix E gives details on the shape functions for the Gauss-Legendre formula and the Newton-Cotes formula.

Numerical Results

Description of Finite-Element Models

To develop the finite-element models used in the analysis of the Space Shuttle nose-gear tire, the cubic spline approximation of the outer meridional surface of the tire half cross section was discretized into 75 potential node points as indicated in figure 5. From this population of possible nodes, a smaller number of nodes was chosen to approximate the tire cross section. To model the tire inflation response, a single strip of 30 finite elements was used to approximate the complete tire cross section. This model employed 61 nodes to characterize the tire meridian, and 480 stress-resultant parameters and 293 nonzero generalized displacement parameters were used to synthesize the tire inflation response.

Finite-element models employed to analyze the contact behavior and friction characteristics of the Space Shuttle nose-gear tire used 41 node points in one half of a meridional cross section (81 nodes for the entire cross section), and these nodes are denoted as the circular symbols in figure 5. Nodes associated with the circumferential tread grooves are also highlighted in figure 5. In the meridional direction, the tread area of the tire was modeled with the highest density of nodes and the sidewall and bead areas were modeled with progressively fewer nodes. This meridional node pattern was used for each of the two-dimensional finite-element tire models employed in this investigation. The circumference of the tire was divided into 240 possible node points, and a smaller number of nodes was chosen from that population to construct the tire finite-element models. To refine the mesh in specific areas such as the contact zone, a higher density of nodes was chosen from the population in the specific region of interest.

Figure 6 shows a map of elements and node locations for one of the models used to analyze the contact problem. Figure 6 shows an array of elements with 40 elements in the meridional direction and 18 elements

in the circumferential direction. Numbers in the left and right margins of figure 6 denote the beginning and ending element numbers in specific rows. Black dots superimposed over the square grid of elements denote the individual nodes of the finite-element model. Several individual elements are shaded and shown in an expanded scale to illustrate the node numbering sequence that is used to minimize the bandwidth for the finite-element models. The complicating factor here is that the elements in the circumferential direction are joined along the top and bottom edge. The numbering scheme that is illustrated in the example shown in figure 6 provides a minimum bandwidth for this tire model. For this specific example the bandwidth is 1635. The six rows of elements in the middle of the array, containing elements 1 through 240, comprise the possible contact region for this model. Figure 6 also shows the location of the circumferential tread grooves of the Space Shuttle nose-gear tire.

Three different models were used in the analysis of the Space Shuttle nose-gear tire in contact with a flat plate. These models, denoted as model 1, model 2, and model 3, are depicted in figure 7. Each model employed 480 elements in the region outside the contact zone ($\theta < 0.2\pi, \theta > 0.2\pi$). Model 1 included 240 elements in the contact region of the tire ($-0.2\pi \le \theta \le 0.2\pi$) for a total of 720 elements. (See fig. 6.) For model 1 there were 14 076 nonzero generalized displacement parameters, 23 040 stress-resultant parameters, and 3159 contact-load intensity parameters. Model 2 used a refined mesh within the contact region with 480 contact elements and a total of 960 elements overall. For model 2 there were 18 776 nonzero generalized displacement parameters, 30 720 stress-resultant parameters, and 6075 contact-load intensity parameters. Model 3 employed a more refined mesh in the contact zone with 960 contact elements and a total of 1440 elements. Model 3 employed 28 152 generalized displacement parameters, 46 080 stress-resultant parameters, and 11 907 contact load-intensity parameters. A single iteration for model 1 required about 12 min on a Cray 2 computer, and a single iteration for model 3 required about 12 min on a Cray Y-MP computer.

Convergence Characteristics and Performance of Contact-Friction Algorithm

Relaxation parameter and penalty parameter effects. Table 2 shows the effect of variations in the relaxation parameter ε_{relax} on the convergence characteristics of the contact-friction algorithm. To study this effect four values of ε_{relax} were evaluated over seven load steps. For a relaxation parameter value of 1.0 no convergence was obtained within 40 iterations beyond the second load step. It should be noted that the first load step, which computed the inflation solution, involved no contact and the second load step involved contact with no sliding. Load steps 3–7 involved some tire sliding for the conditions summarized in table 2. A relaxation parameter value of 0.75 required a total of 104 iterations to obtain converged solutions at the seven load steps; for a value of ε_{relax} of 0.5, only 36 iterations were required to cover the same load range; and a relaxation parameter value of 0.25 required a total of 149 iterations. It is obvious from these results that the choice of the relaxation parameter can have a profound effect on the convergence characteristics of the contact-friction algorithm.

Data shown in table 3 illustrate the oscillating frictional load intensities that were observed when the relaxation parameter was set to 0.75. In table 3 both the lateral friction load intensity and the drag friction load intensity are shown to change sign 13 times during the course of the 28 iterations required to obtain a converged solution at the third load step. No oscillatory behavior was observed for the friction-force load intensities when the relaxation parameter was set to 0.5 or 0.25.

Table 4 summarizes the effect of tangential penalty parameter variations on convergence characteristics of the contact-friction algorithm. To evaluate this effect four values of ε_t were studied over seven load steps. For a tangential penalty parameter value of 1.0 a total of 31 iterations was required to obtain converged solutions over the range of load steps tested. At a tangential penalty parameter value of 10^{12} the number of iterations required to obtain converged solutions over the same load range increased to 45. Thus, approximately a 50 percent increase in iterations was required for converged solutions when ε_t was increased by 12 orders of magnitude.

The physical significance of the tangential penalty parameter is that it represents the distributed tangential stiffness of the tire-contact interface and therefore serves a double role of penalty parameter and tire stiffness parameter in the contact-friction algorithm. When ε_t is set to a value of 1.0, the footprint of the contact-friction algorithm is compliant; little or no slip occurs in the tire contact zone and the predicted friction-force load intensities are very small. When ε_t is set to 10^{12} the footprint of the contact-friction algorithm is extremely stiff, the tire must undergo slip to satisfy the Coulomb friction law constraint, and the calculated friction-force load intensities may be too high. To illustrate this point more clearly, figure 8 shows the normalized tire slip dissipation energies in the lateral and drag directions for two values of ε_t. Figure 8 indicates that the amount of energy dissipated by the tire due to slipping in the footprint is strongly influenced by the choice of ε_t. Data presented in figure 8

also indicate that the contact-friction algorithm predicts much more energy dissipated from lateral slipping by the tire than from slipping in the drag direction for static loading cases studied in this investigation.

Figure 9 presents the influence of normal penalty parameter magnitude on the accuracy of total strain energy and total contact force. Total strain energy is the integral of total strain energy density over the full extent of the tire carcass, while total contact force is the integral of normal contact-load intensity over the entire contact zone. Strain-energy ratio, denoted by the solid line, and contact-force ratio, denoted by the dashed line, are plotted as a function of the base 10 logarithm of the penalty parameter in figure 9. Results in figure 9 indicate that total calculated strain energy and total contact force are insensitive to variations in the normal penalty parameter over the range of 10^6 to 10^{15}. It should be noted that for these tire-contact problems, total contact force is much more sensitive to a poor choice in the penalty parameter than total strain energy, as denoted by the percent errors on the two ordinate axes.

Friction coefficient and load step size effects. Table 5 summarizes the effect of static and dynamic friction coefficient variations on convergence characteristics of the contact-friction algorithm. Three different static friction coefficients were evaluated to study these effects. $\mu_{static} = 0.3$ represents a wet concrete runway condition; $\mu_{static} = 0.6$ represents a dry concrete runway condition; and $\mu_{static} = 1.0$ represents a maximum friction coefficient associated with aircraft tires in general. The dynamic friction coefficient for each friction state was taken to be 85 percent of the static value. These friction coefficient values are consistent with a substantial aircraft tire friction database that has been acquired over a number of years. Reference 33 gives further details on experimental friction measurements for aircraft tires and empirical relationships for predicting aircraft tire friction responses. Data in table 5 indicate that about 30 percent more iterations were required to obtain converged solutions over the range of load steps tested for the low friction surface and the high friction surface than for the friction coefficients representative of the dry runway condition. These results indicate that the contact-friction algorithm is robust enough to handle the range of friction coefficients normally experienced in aircraft tire applications.

Table 6 summarizes the effects of varying load step size on the convergence characteristics of the contact-friction algorithm. This study evaluates performance of the algorithm over a normal tire deflection range from 0 to 0.6 in. In the first case the tire deflection range was covered in 10 load steps; in the second case this deflection range was covered in 5 load steps; and in the third case the deflection range was covered in 4 load steps. Case 1 required 52 iterations and computed a tire load of 3998 lb for a tire deflection of 0.6 in. Case 2 required 28 iterations and case 3 required 26 iterations to obtain a converged solution at a tire deflection of 0.6 in. The calculated normal tire load for case 2 was 0.6 percent less than the predicted load of case 1 and the calculated normal load for case 3 was 0.9 percent less than that for case 1. It appears that the contact-friction algorithm can operate over a range of step sizes without serious degradation in performance.

Conclusions

A computational procedure is presented for the solution of frictional contact problems for aircraft tires. The Space Shuttle nose-gear tire was modeled using a two-dimensional laminated anisotropic shell theory which includes the effects of variation in material and geometric parameters, transverse-shear deformation, and geometric nonlinearities. Contact conditions were incorporated into the formula by using a perturbed Lagrangian approach with the fundamental unknowns consisting of stress resultants, generalized displacements, and Lagrange multipliers associated with contact and friction conditions. The contact-friction algorithm is based on a modified Coulomb friction law. A modified two-field, mixed-variational principle was used to obtain elemental arrays. This modification consists of augmenting the functional of that principle by two terms: the Lagrange multiplier vector associated with normal and tangential node contact load intensities and a regularization term that is quadratic in the Lagrange multiplier vector.

Shape functions used in approximating generalized displacements and Lagrange multipliers were selected to be the same and differ from those used to approximate stress resultants. Stress resultants and Lagrange multipliers were allowed to be discontinuous at the interelement boundaries. Nonlinearities due to large displacements, moderate rotations, and contact conditions were combined into the same iteration loop and were handled by using the Newton-Raphson iterative scheme.

Numerical results are presented for the Space Shuttle nose-gear tire subjected to inflation pressure loads and combined inflation pressure and contact loads against a rigid flat plate.

Results from this investigation lead to the following observations and conclusions: (1) the choice of the relaxation parameter is critical to the performance of the contact-friction algorithm. If the parameter is too large, oscillating friction load intensities occur; if the parameter is too small, many iterations are required for

convergence. (2) The tangential penalty parameter is a measure of tangential stiffness of the tire-contact interface and has a strong influence on energy dissipated by the tire due to slip. Normal contact-load intensity distribution and strain energy are insensitive to variations in the normal penalty parameter. (3) The contact-friction algorithm is robust enough to handle the range of friction coefficients associated with aircraft tire applications.

NASA Langley Research Center
Hampton, VA 23681-0001
January 18, 1996

Appendix A

Fundamental Equations of Shell Theory Used in Present Study

Appendix A summarizes the fundamental equations of the Sanders-Budiansky type shell of revolution used in this study. Effects of laminated, anisotropic material response and transverse-shear deformation are included in these relationships.

Strain-Displacement Relationships

$$\varepsilon_s = \partial_s u + \frac{w}{R_1} + \underline{\frac{1}{2}\left(\frac{u}{R_1} - \partial_s w\right)^2} + \frac{1}{2}\phi^2 \tag{A1}$$

$$\varepsilon_\theta = \frac{\partial_s r}{r} u + \frac{1}{r}\partial_\theta v + \frac{w}{R_2} + \underline{\frac{1}{2}\left(\frac{v}{R_2} - \frac{1}{r}\partial_\theta w\right)^2} + \frac{1}{2}\phi^2 \tag{A2}$$

$$2\varepsilon_{s\theta} = \frac{1}{r}\partial_\theta u + \left(\partial_s - \frac{\partial_s r}{r}\right)v + \underline{\left(\frac{u}{R_1} - \partial_s w\right)\left(\frac{v}{R_2} - \frac{1}{r}\partial_\theta w\right)} \tag{A3}$$

$$\kappa_s = \partial_s \phi_s \tag{A4}$$

$$\kappa_\theta = \frac{\partial_s r}{r}\phi_s + \frac{1}{r}\partial_\theta \phi_\theta \tag{A5}$$

$$2\kappa_{s\theta} = \frac{1}{r}\partial_\theta \phi_s + \left(\partial_s - \frac{\partial_s r}{r}\right)\phi_\theta + \left(\frac{1}{R_2} - \frac{1}{R_1}\right)\phi \tag{A6}$$

$$2\varepsilon_{s3} = -\frac{u}{R_1} + \partial_s w + \phi_s \tag{A7}$$

$$2\varepsilon_{\theta 3} = -\frac{v}{R_2} + \frac{1}{r}\partial_\theta w + \phi_\theta \tag{A8}$$

where ε_s and ε_θ are extensional strains in the meridional and circumferential directions, $2\varepsilon_{s\theta}$ is the in-plane shear strain, κ_s and κ_θ are bending strains in the meridional and circumferential directions, $2\kappa_{s\theta}$ is the twisting strain, $2\varepsilon_{s3}$ and $2\varepsilon_{\theta 3}$ are transverse-shear strains, $\partial_s \equiv \frac{\partial}{\partial_s}$, $\partial_\theta \equiv \frac{\partial}{\partial_\theta}$, and ϕ is the rotation around the normal to the shell, which is given by

$$\phi = \left[-\frac{1}{r}\partial_\theta u + \left(\partial_s + \frac{\partial_s r}{r}\right)v\right] \tag{A9}$$

Nonlinear terms that account for moderate rotations are underlined with dashes in equations (A1) to (A3).

Constitutive Relations

The shell is assumed to be made of a laminated, anisotropic, linearly elastic material. Every point of the shell is assumed to possess a single plane of elastic symmetry parallel to the middle surface. The relationships between the stress resultants and the strain measures of the shell are given by

$$\begin{Bmatrix} N_s \\ N_\theta \\ N_{s\theta} \\ \hdashline M_s \\ M_\theta \\ M_{s\theta} \\ \hdashline Q_s \\ Q_\theta \end{Bmatrix} = \left[\begin{array}{ccc:ccc:cc} c_{11} & c_{12} & \textcircled{c_{16}} & f_{11} & f_{12} & \textcircled{f_{16}} & \bullet & \bullet \\ & c_{22} & \textcircled{c_{26}} & f_{12} & f_{22} & \textcircled{f_{26}} & \bullet & \bullet \\ & & c_{66} & \textcircled{f_{16}} & \textcircled{f_{26}} & f_{66} & \bullet & \bullet \\ \hdashline & & & d_{11} & d_{12} & \textcircled{d_{16}} & \bullet & \bullet \\ & & & & d_{22} & \textcircled{d_{26}} & \bullet & \bullet \\ & \text{Symmetric} & & & & d_{66} & \bullet & \bullet \\ \hdashline & & & & & & c_{55} & \textcircled{c_{45}} \\ & & & & & & & c_{44} \end{array}\right] \begin{Bmatrix} \varepsilon_s \\ \varepsilon_\theta \\ 2\varepsilon_{s\theta} \\ \hdashline \kappa_s \\ \kappa_\theta \\ 2\kappa_{s\theta} \\ \hdashline 2\varepsilon_{s3} \\ 2\varepsilon_{\theta 3} \end{Bmatrix} \tag{A10}$$

where c_{ij}, f_{ij}, and d_{ij} $(i, j = 1, 2, 6)$ are shell stiffness coefficients. Nonorthotropic (anisotropic) terms are circled and dots indicate zero terms.

Appendix B

Formulas for Elemental Arrays $[F]$, $[S]$, $[G(X)]$, $[M(H, X)]$, $[P]$, $[Q]$, $[R]$, and $\{g_0\}$

Appendix B gives explicit forms of the elemental arrays $[F]$, $[S]$, $[G(X)]$, $[M(H, X)]$, and $[P]$. The arrays are partitioned into blocks corresponding to the contributions from individual nodes or stress-resultant approximation functions. Expressions for the typical blocks are given in table B1. The order of the strains is ε_s, ε_θ, $2\varepsilon_{s\theta}$, κ_s, κ_θ, $2\kappa_{s\theta}$, $2\varepsilon_{s3}$, and $2\varepsilon_{\theta 3}$. The order of the nodal displacement parameters is u, v, w, ϕ_s, and ϕ_θ.

In table B1, $\bar{N}^k$ and $\bar{N}^l$ are shape functions associated with stress-resultant components; N^i and N^j are shape functions for generalized displacements; s is the number of stress nodes in the element; m is the number of displacement nodes in the element; and $\Omega^{(e)}$ is the element domain. The range of the indices k and l is 1 to s; the range of the indices i and j is 1 to m. Dots in the matrices refer to zero terms; $\partial_s \equiv \frac{\partial}{\partial_s}$; and $\partial_\theta \equiv \frac{\partial}{\partial_\theta}$. Quantities $\bar{\varepsilon}_1$ and $\bar{\varepsilon}_2$ are defined in terms of

$$\bar{\varepsilon}_1 = \frac{u}{R_1} - \partial_s w \tag{B1}$$

$$\bar{\varepsilon}_2 = \frac{u}{R_2} - \frac{1}{r}\partial_\theta w \tag{B2}$$

Table B1. Explicit Form of Typical Partitions of Arrays $[F]$, $[S]$, $[G(X)]$, $[M(H, X)]$, and $[P]$

Array	Number of partitions (or blocks)	Typical partition
$[F]_{kl}$	$s \times s$	$\int_{\Omega^{(e)}} \overline{N}^k \overline{N}^l = \begin{bmatrix} a_{11} & a_{12} & a_{16} & b_{11} & b_{12} & b_{16} & \bullet & \bullet \\ & a_{22} & a_{26} & b_{12} & b_{22} & b_{26} & \bullet & \bullet \\ & & a_{66} & b_{16} & b_{26} & b_{66} & \bullet & \bullet \\ & & & g_{11} & g_{12} & g_{16} & \bullet & \bullet \\ & & \text{Symmetric} & & g_{22} & g_{26} & \bullet & \bullet \\ & & & & & g_{66} & \bullet & \bullet \\ & & & & & & a_{ss} & a_{s\theta} \\ & & & & & & & a_{\theta\theta} \end{bmatrix} d\Omega$
$[S]_{kj}$	$s \times m$	$\int_{\Omega^{(e)}} \overline{N}^k \begin{bmatrix} \partial_s & \bullet & \frac{1}{R_1} & \bullet & \bullet \\ \frac{\partial_s r}{r} & \frac{1}{r}\partial_\theta & \frac{1}{R_2} & \bullet & \bullet \\ \frac{1}{r}\partial_\theta & \partial_s - \frac{\partial_s r}{r} & \bullet & \bullet & \bullet \\ \bullet & \bullet & \bullet & \partial_s & \bullet \\ \bullet & \bullet & \bullet & \frac{\partial_s r}{r} & \frac{1}{r}\partial_\theta \\ \frac{1}{2r}\left(\frac{1}{R_1} - \frac{1}{R_2}\right)\partial_\theta & -\frac{1}{2}\left(\frac{1}{R_1} - \frac{1}{R_2}\right)\left(\partial_s + \frac{\partial_s r}{r}\right) & \bullet & \frac{1}{r}\partial_\theta & \partial_s - \frac{\partial_s r}{r} \\ -\frac{1}{R_1} & \bullet & \partial_s & 1 & \bullet \\ \bullet & -\frac{1}{R_2} & \frac{1}{r}\partial_\theta & \bullet & 1 \end{bmatrix} N^j d\Omega$

Table B1. Concluded

Array	Number of partitions (or blocks)	Typical partition
$\{G(X)\}_k$	s	$\int\limits_{\Omega_{(e)}} \overline{N}^k \left\{ \begin{array}{c} \frac{1}{2}\left(\frac{u}{R_1} - \partial_s w\right)^2 + \frac{1}{2}\phi^2 \\ \frac{1}{2}\left(\frac{v}{R_2} - \frac{1}{r}\partial_\theta w\right)^2 + \frac{1}{2}\phi^2 \\ \left(\frac{u}{R_1} - \partial_s w\right)\left(\frac{v}{R_2} - \frac{1}{r}\partial_\theta w\right) \\ \bullet \\ \bullet \\ \bullet \\ \bullet \\ \bullet \end{array} \right\} d\Omega$
$\{M(H,X)\}_j$	m	$\int\limits_{\Omega^{(e)}} \left\{ \begin{array}{c} \frac{1}{R_1}(N_s\bar{\varepsilon}_1 + N_{s\theta}\bar{\varepsilon}_2) - \frac{1}{2r}(N_s + N_\theta)\phi\partial_\theta \\ \frac{1}{R_2}(N_{s\theta}\bar{\varepsilon}_1 + N_\theta\bar{\varepsilon}_2) + \frac{1}{2}(N_s + N_\theta)\phi\left(\partial_s + \frac{\partial_s r}{r}\right) \\ -(N_s\bar{\varepsilon}_1 + N_{s\theta}\bar{\varepsilon}_2)\partial_s - \frac{1}{r}(N_{s\theta}\bar{\varepsilon}_1 + N_\theta\bar{\varepsilon}_2)\partial_\theta \\ \bullet \\ \bullet \\ \bullet \\ \bullet \\ \bullet \end{array} \right\} N^j d\Omega$
$\{P\}_j$	m	$\int\limits_{\Omega^{(e)}} N^j \left\{ \begin{array}{c} P_s \\ P_\theta \\ P \\ \bullet \\ \bullet \end{array} \right\} d\Omega$

Appendix B also gives explicit forms of elemental arrays $[Q]$, $[R]$, and $\{g_0\}$. Table B2 gives expressions of typical partitions. In table B2, N^i and N^j are shape functions for Lagrange multipliers and generalized displacements and c is the number of nodal points in contact within the element. The range of the indices i and j is from 1 to c, and the range of the index i' is from 1 to m; $<\tilde{g}_w>$ is the unit ramp (or singularity) function defined as follows:

$$<\tilde{g}_w>^n = \begin{cases} \tilde{g}_w^n & (\tilde{g}_w > 0) \\ 0 & (\tilde{g}_w \le 0) \end{cases} \tag{B3}$$

where $\tilde{g}_w = -\tilde{g}_w$ and $n = 0$ or 1. Vector $\{g_0\}$ contains components $\bar{g}_u$, $\bar{g}_v$, and $<\tilde{g}_w>$ for each contact node. Components $\bar{g}_u$ and $\bar{g}_v$ are defined in figure 2(b).

Table B2. Explicit Form of Typical Partitions of Arrays $[Q]$, $[R]$, and $\{g_0\}$

Array	Number of partitions (or blocks)	Formula for typical partition
$[Q]$	$m \times c$	$\int_{\Omega^{(e)}} N^{i'} N^j <\tilde{g}_w>^0 d\Omega$
$[R]$	$c \times c$	$-\int_{\Omega^{(e)}} N^i N^j <\tilde{g}_w>^0 d\Omega$
$\{g_0\}$	c	$\int_{\Omega^{(e)}} N^i \begin{Bmatrix} \bar{g}_u \\ \bar{g}_v \\ <\tilde{g}_w> \end{Bmatrix} d\Omega$

Appendix C

Derivation of Newton-Raphson Tangential Operator Equations

Taylor's Series Preliminary Discussion

The governing differential equations for the tire contact problem are

$$\begin{bmatrix} -f_l & s_l & \bullet \\ s_l^t & \bullet & q_c \\ \bullet & q_c^t & \dfrac{r_c}{\varepsilon} \end{bmatrix}^{(e)} \begin{Bmatrix} h \\ x \\ \lambda \end{Bmatrix}^{(e)} + \begin{Bmatrix} \frac{1}{2} m_{nl} xx \\ m_{nl} xh \\ \bullet \end{Bmatrix}^{(e)} - \begin{Bmatrix} \bullet \\ pP \\ g_0 \end{Bmatrix}^{(e)} = 0 \tag{C1}$$

In equation (C1) f_l is the element flexibility matrix, dimensioned $s8 \times s8$ and partitioned into $s \times s$ submatrices; s_l is the element linear strain-displacement matrix, dimensioned $s8 \times m5$ and partitioned into $s \times m$ submatrices; m_{nl} is the element stress-displacement displacement matrix, dimensioned $s3m3 \times m3$ and partitioned into $sm \times m$ submatrices; and q_c and r_c are matrices associated with contact, dimensioned $m \times c3$ and $c \times c3$ and partitioned into $m \times c$ and $c \times c$ submatrices, respectively. Subvectors h, x, and λ representing stress, displacement, and contact-load intensity are dimensioned s, m, and $c3$, respectively. The normalized external load vector P is dimensioned $m5$ and the vector of initial gaps g_0 is dimensioned $c3$. The penalty parameter is denoted as ε and the loading parameter is denoted as p. Superscript t denotes transpose and superscript (e) indicates that the equations are developed at the element level. Equation (C1) can be expressed as three functions by carrying out the indicated multiplication:

$$f(h, x, \lambda) = -f_l h + s_l x + \frac{1}{2} m_{nl} xx = 0 \tag{C2}$$

$$g(h, x, \lambda) = s_l^t h + q_c \lambda + m_{nl} xh - pP = 0 \tag{C3}$$

$$j(h, x, \lambda) = q_c^t x + \left(\frac{r_c}{\varepsilon}\right)\lambda + g_0 = 0 \tag{C4}$$

Consider a point x_0 "reasonably" close to a root of a function $f(x)$. Taylor's series expansion about x_0 is

$$f(x) = f(x_0) + (x - x_0) f'(x_0) + \left(\frac{1}{2!}\right)(x - x_0)^2 f''(x_0) + \ldots \tag{C5}$$

If $f(x)$ is set to zero, then x is a root of the right-hand side of the Taylor series expansion about x_0 (taking linear terms only):

$$0 = f(x_0) + (x - x_0) f'(x_0) \tag{C6}$$

$$(x - x_0) f'(x_0) = -f(x_0) \tag{C7}$$

$$x = x_0 - \frac{f(x_0)}{f'(x_0)} \tag{C8}$$

or

$$x - x_0 = \delta = -\frac{f(x_0)}{f'(x_0)} \tag{C9}$$

x represents an improved estimate of the root to replace x_0

$$x^{(n+1)} = x^n + \delta^{(n+1)} \tag{C10}$$

Taylor's series expansion of equation (C1) about h_0, x_0, and λ_0, considering the linear terms only, leads to the following:

$$f(h, x, \lambda) = f(h_0, x_0, \lambda_0) + (h - h_0)\frac{\partial f}{\partial h} + (x - x_0)\frac{\partial f}{\partial x} + (\lambda - \lambda_0)\frac{\partial f}{\partial \lambda} \tag{C11}$$

$$g(h, x, \lambda) = g(h_0, x_0, \lambda_0) + (h - h_0)\frac{\partial g}{\partial h} + (x - x_0)\frac{\partial g}{\partial x} + (\lambda - \lambda_0)\frac{\partial g}{\partial \lambda} \tag{C12}$$

$$j(h, x, \lambda) = j(h_0, x_0, \lambda_0) + (h - h_0)\frac{\partial j}{\partial h} + (x - x_0)\frac{\partial j}{\partial x} + (\lambda - \lambda_0)\frac{\partial j}{\partial \lambda} \tag{C13}$$

Case I—No Contact

Consider first the case for no contact where equation (C1) is reduced to

$$\begin{bmatrix} -f_l & s_l \\ s_l^t & \bullet \end{bmatrix} \begin{Bmatrix} h \\ x \end{Bmatrix} + \begin{Bmatrix} \frac{1}{2} m_{nl} xx \\ m_{nl} xh \end{Bmatrix} - \begin{Bmatrix} \bullet \\ pP \end{Bmatrix} = 0 \tag{C14}$$

$$-f_l h + s_l x + \frac{1}{2} m_{nl} xx = 0 \tag{C15}$$

$$s_l^t h + m_{nl} xh - pP = 0 \tag{C16}$$

and rearranging the nonlinear terms

$$\begin{bmatrix} -f_l & \left(s_l + \frac{1}{2} m_{nl} x\right) \\ (s_l^t + m_{nl} x) & \bullet \end{bmatrix} \begin{Bmatrix} h \\ x \end{Bmatrix} - \begin{Bmatrix} \bullet \\ pP \end{Bmatrix} = 0 \tag{C17}$$

Applying the Taylor series expansion yields the following equations:

$$-f_l h_0 + s_l x_0 + \frac{1}{2} m_{nl} x_0 x_0 - (h - h_0) f_l + (x - x_0)(s_l + m_{nl} x_0) = 0 \tag{C18}$$

$$s_l^t h_0 + m_{nl} x_0 h_0 - pP + (h - h_0)(s_l^t + m_{nl} x_0) + (x - x_0) m_{nl} h_0 = 0 \tag{C19}$$

Let

$$(h - h_0) = \Delta h \tag{C20}$$

and

$$(x - x_0) = \Delta x \tag{C21}$$

Equations (C18) and (C19) become

$$\begin{bmatrix} -f_l & (s_l + m_{nl}x_0) \\ (s_l^t + m_{nl}x_0) & m_{nl}h_0 \end{bmatrix} \begin{Bmatrix} \Delta h \\ \Delta x \end{Bmatrix} = \begin{Bmatrix} f_l h_0 - s_l x_0 - \frac{1}{2} m_{nl} x_0 x_0 \\ -s_l^t h_0 - m_{nl} x_0 h_0 + pP \end{Bmatrix} = \begin{Bmatrix} rh \\ rx \end{Bmatrix} \tag{C22}$$

Equation (C22) defines the tangent operator for the Newton-Raphson iterative solution procedure for problems that do not involve contact. Looking at the first part of equation (C22) where

$$-f_l \Delta h + (s_l + m_{nl}x_0)\Delta x = f_l h_0 - s_l x_0 - \frac{1}{2} m_{nl} x_0 x_0 = rh \tag{C23}$$

then multiplying by the inverse of the flexibility matrix

$$-\Delta h + f_l^{-1}(s_l + m_{nl}x_0)\Delta x = h_0 - f_l^{-1} s_l x_0 - \frac{1}{2} f_l^{-1} m_{nl} x_0 x_0 = f_l^{-1} rh \tag{C24}$$

and then substituting into the second part of equation (C22) yields

$$(s_l^t + m_{nl}x_0) f_l^{-1}(s_l + m_{nl}x_0)\Delta x + m_{nl}h_0 \Delta x = -s_l^t h_0 - m_{nl}x_0 h_0 + pP - (s_l^t + m_{nl}x_0) f_l^{-1} rh = rx - (s_l^t + m_{nl}x_0) f_l^{-1} rh \tag{C25}$$

Equation (C25) is the governing differential equation for problems that do not involve contact with the stresses eliminated. Equation (C25) can be rewritten by defining the following terms that are employed in the tire modeling code used in this investigation:

$$[k_{22}] = m_{nl}h_0 \tag{C26}$$

$$[k_{12}\text{bar}] = f_l^{-1}(s_l + m_{nl}x_0) \tag{C27}$$

$$[k_{12}s]^t = (s_l + m_{nl}x_0) \tag{C28}$$

$$(\text{rhbar}) = f_l^{-1} rh \tag{C29}$$

and equation (C25) now becomes

$$([k_{12}s]^t [k_{12}\text{bar}] + [k_{22}])\Delta x = (rx) - [k_{12}s]^t (\text{rhbar}) \tag{C30}$$

Case II—Contact

Next consider the case of contact by reintroducing the contact terms into equation (C17)

$$\begin{bmatrix} -f_l & \left(s_l + \frac{1}{2} m_{nl} x\right) & \bullet \\ (s_l^t + m_{nl}x) & \bullet & q_c \\ \bullet & q_c^t & \frac{r_c}{\varepsilon} \end{bmatrix} \begin{Bmatrix} h \\ x \\ \lambda \end{Bmatrix} - \begin{Bmatrix} \bullet \\ pP \\ g_0 \end{Bmatrix} = 0 \tag{C31}$$

Applying the Taylor series expansion yields

$$-f_l h_0 + s_l x_0 + \frac{1}{2} m_{nl} x_0 x_0 - (h - h_0) f_l + (x - x_0)(s_l + m_{nl}x_0) = 0 \tag{C18}$$

$$s_l^t h_0 + m_{nl} x_0 h_0 + q_c \lambda_0 - pP + (h - h_0)(s_l^t + m_{nl} x_0) + (x - x_0) m_{nl} h_0 + (\lambda - \lambda_0) q_c \;=\; 0 \tag{C32}$$

$$q_c^t x_0 + \frac{r_c}{\varepsilon}\lambda_0 - g_0 + (x - x_0) q_c^t + (\lambda - \lambda_0)\frac{r_c}{\varepsilon} \;=\; 0 \tag{C33}$$

Let

$$(\lambda - \lambda_0) \;=\; \Delta\lambda \tag{C34}$$

Equations (C18), (C32), and (C33) become

$$\begin{bmatrix} -f_l & (s_l + m_{nl} x_0) & \bullet \\ (s_l^t + m_{nl} x_0) & \bullet & q_c \\ \bullet & q_c^t & \dfrac{r_c}{\varepsilon} \end{bmatrix} \begin{Bmatrix} \Delta h \\ \Delta x \\ \Delta\lambda \end{Bmatrix} = \begin{Bmatrix} f_l h_0 - s_l x_0 - \dfrac{1}{2} m_{nl} x_0 x_0 \\ -s_l^t h_0 - m_{nl} x_0 h_0 - q_c \lambda_0 + pP \\ -q_c^t x_0 - \dfrac{r_c}{\varepsilon}\lambda_0 + g_0 \end{Bmatrix} = \begin{Bmatrix} rh \\ rx \\ r\lambda \end{Bmatrix} \tag{C35}$$

The contact equation (the last part of eq. (C35)) can be written as

$$\left(\frac{r_c}{\varepsilon}\right)\Delta\lambda \;=\; -q_c^t \Delta x - q_c^t x_0 - \frac{r_c}{\varepsilon}\lambda_0 + g_0 \tag{C36}$$

and solving for $\Delta\lambda$ yields

$$\Delta\lambda \;=\; -\left(\frac{r_c}{\varepsilon}\right)^{-1} q_c^t \Delta x - \left(\frac{r_c}{\varepsilon}\right)^{-1} q_c^t x_0 + \left(\frac{r_c}{\varepsilon}\right)^{-1} g_0 - \lambda_0 \tag{C37}$$

Substituting equation (C37) into the second part of equation (C35) redefines the governing differential equation to account for contact terms

$$\begin{aligned} (s_l^t + m_{nl} x_0) f_l^{-1} (s_l + m_{nl} x_0)\Delta x + m_{nl} h_0 \Delta x - \underline{q_c \left(\frac{r_c}{\varepsilon}\right)^{-1} q_c^t \Delta x} \;&=\; -s_l^t h_0 - m_{nl} x_0 h_0 + pP - (s_l^t + m_{nl} x_0) f_l^{-1} rh - \underline{q_c \left(\frac{r_c}{\varepsilon}\right)^{-1} (g_0 - q_c^t x_0)} \\ &=\; rx - (s_l^t + m_{nl} x_0) f_l^{-1} rh - \underline{q_c \left(\frac{r_c}{\varepsilon}\right)^{-1} (g_0 - q_c^t x_0)} \end{aligned} \tag{C38}$$

where the underlined terms are those associated with contact. Equation (C38) is identical to equation (8) in the main body of the paper. The following terms are associated with the contact solution in the tire modeling code used in this investigation:

$$[\text{dlbar}] \;=\; \left(\frac{r_c}{\varepsilon}\right)^{-1} q_c^t \tag{C39}$$

$$(\text{rlbar}) \;=\; \left(\frac{r_c}{\varepsilon}\right)^{-1} (g_0 - q_c^t x_0) - \lambda_0 \tag{C40}$$

$$(\text{rlb}) \;=\; \left(\frac{r_c}{\varepsilon}\right)^{-1} (g_0 - q_c^t x_0) \tag{C41}$$

and equation (C38) can be rewritten as

$$([k_{12}s]^t [k_{12}\text{bar}] + [k_{22}] - \underline{q_c [\text{dlbar}]})\Delta x \;=\; (rx) - [k_{12}s]^t (\text{rhbar}) - \underline{q_c (\text{rlb})} \tag{C42}$$

where the underlined terms are associated with contact. The stresses are recovered from the displacement solution through the following equation:

$$(h) = (\text{rhbar}) - [k_{12}\text{bar}](x) \tag{C43}$$

and the contact-load intensities are recovered from the displacement solution with

$$(\lambda) = (\text{rlbar}) - [\text{dlbar}](x) \tag{C44}$$

Appendix D

Transformation of Elemental Arrays From Shell Coordinates to Global Cartesian Coordinates

Transformation of the displacement components from the shell coordinates (s, θ, x_3) to the global Cartesian coordinates (x, y, z) is expressed by the following equation:

$$\{X\}^{(e)} = [T]\{\bar{X}\}^{(e)} \tag{D1}$$

where $[T]$ is a block-diagonal transformation whose submatrix at each node is given by

$$\underset{(5\times 5)}{[T]^{(n)}} = \begin{bmatrix} \hat{e}_s & \hat{e}_\theta & \hat{e}_s \times \hat{e}_\theta & \vec{0} & \vec{0} \\ & & & 1 & 0 \\ & & \leftarrow 0 & & \\ & & & 0 & 1 \end{bmatrix} \tag{D2}$$

where $\hat{e}_s$ and $\hat{e}_\theta$ are tangential unit vectors in the s- and θ-directions, respectively, $\vec{0}$ is the null vector, and $\{X\}^{(e)}$ and $\{\bar{X}\}^{(e)}$ are generalized displacements in shell coordinates and global Cartesian coordinates, respectively. Note that rotation components ϕ_s and ϕ_θ are not transformed since the outer surface of the tire was chosen as the reference surface; therefore, ϕ_s and ϕ_θ do not appear in the contact conditions.

Elemental matrices $[S]$ and $\left[\frac{\partial M}{\partial \bar{X}}\right]$ and the external load vector $\{P\}$ are transformed from the shell coordinates to the global Cartesian coordinates as follows:

$$[S] \rightarrow [S][T] \tag{D3}$$

$$\left[\frac{\partial M}{\partial \bar{X}}\right] \rightarrow [T]^t \left[\frac{\partial M}{\partial \bar{X}}\right][T] \tag{D4}$$

$$\{P\} \rightarrow [T]^t\{P\} \tag{D5}$$

Nonlinear vectors $\{G(X)\}$ and $\{M(H, X)\}$ are evaluated with displacement vector $\{X\}$ expressed in terms of $\{\bar{X}\}$ at the end of each iteration cycle.

Appendix E

Details of Shape Functions for M9-4 Finite-Element Model

Appendix E presents the expressions for the shape functions used in the M9-4 finite-element model in terms of the local quadrilateral (or natural) coordinates ξ and η. In figure E1 the open circular symbols denote the nine nodes for the generalized displacements and Lagrange multipliers, and the filled symbols denote the interior nodes for the stress resultants. Figure E1 also lists the coordinates of the four corner nodes.

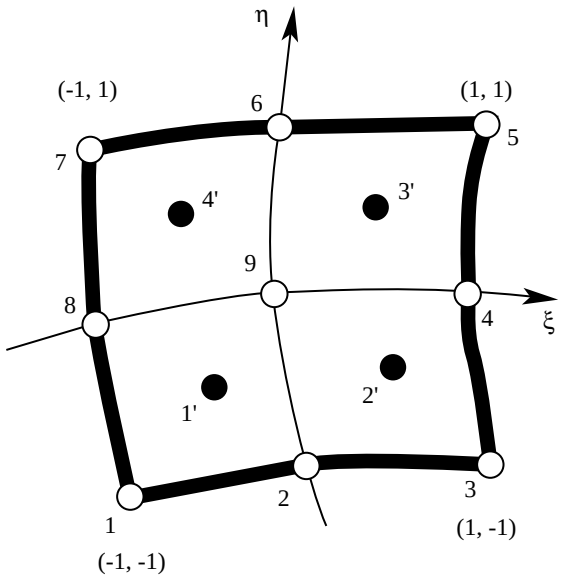

Figure E1. Schematic of the M9-4 finite element.

Shape functions for the biquadratic approximations are given by the following system of equations:

$$
\begin{aligned}
N^1 &= \frac{1}{4}\xi\eta(\xi-1)(\eta-1) \\
N^2 &= \frac{1}{2}\eta(1-\xi^2)(\eta-1) \\
N^3 &= \frac{1}{4}\xi\eta(\xi+1)(\eta-1) \\
N^4 &= \frac{1}{2}\xi(\xi+1)(1-\eta^2) \\
N^5 &= \frac{1}{4}\xi\eta(\xi+1)(\eta+1) \\
N^6 &= \frac{1}{2}\eta(1-\xi^2)(\eta+1) \\
N^7 &= \frac{1}{4}\xi\eta(\xi-1)(\eta+1) \\
N^8 &= \frac{1}{2}\xi(\xi-1)(1-\eta^2) \\
N^9 &= (1-\xi^2)(1-\eta^2)
\end{aligned}
\tag{E1}
$$

When the stress nodes are located at the center of each element quadrant, the corresponding bilinear shape functions for the stress resultants are given by

$$\bar{N}^{1'} = \frac{1}{4}(1 - 2\xi - 2\eta + 4\xi\eta)$$

$$\bar{N}^{2'} = \frac{1}{4}(1 + 2\xi - 2\eta - 4\xi\eta)$$

$$\bar{N}^{3'} = \frac{1}{4}(1 + 2\xi + 2\eta + 4\xi\eta)$$

$$\bar{N}^{4'} = \frac{1}{4}(1 - 2\xi + 2\eta - 4\xi\eta) \qquad \text{(E2)}$$

Elemental arrays $[F]$, $[S]$, $\{G(X)\}$, $\{M(H,X)\}$, and $\{P\}$ are evaluated numerically using a Gauss-Legrendre formula, and the arrays $[Q]$, $[R]$, and $\{g_0\}$ are evaluated using a Newton-Cotes formula. Reference 34 describes these numerical quadrature formulas.

References

1. Zhong, Zhi-Hua; and Mackerle, Jaroslav: Static Contact Problems—A Review. *Eng. Comput*., vol. 9, Feb. 1992, pp. 3–37.

2. Tanner, John A.; Stubbs, Sandy M.; and McCarty, John L.: *Static and Yawed-Rolling Mechanical Properties of Two Type VII Aircraft Tires*. NASA TP-1863, 1981.

3. Stubbs, Sandy M.; Tanner, John A.; and Smith, Eunice G.: *Behavior of Aircraft Antiskid Braking Systems on Dry and Wet Runway Surfaces—A Slip-Velocity-Controlled, Pressure-Bias-Modulated System*. NASA TP-1051, 1979.

4. Tanner, John A.; Dreher, Robert C.; Stubbs, Sandy M.; and Smith, Eunice G.: *Tire Tread Temperatures During Antiskid Braking and Cornering on a Dry Runway.* NASA TP-2009, 1982.

5. Daugherty, Robert H.; and Stubbs, Sandy M.: *Cornering and Wear Behavior of the Space Shuttle Orbiter Main Gear Tire*. SAE Paper 871867, Oct. 1987.

6. Daugherty, Robert H.; and Stubbs, Sandy M.: *Spin-Up Studies of the Space Shuttle Orbiter Main Gear Tire*. SAE Paper 881360, Oct. 1988.

7. Oden, J. T.; and Martins, J. A. C.: Models and Computational Methods for Dynamic Friction Phenomena. *Comput. Methods Appl. Mech. & Eng.*, vol. 52, nos. 1–3, Sept. 1985, pp. 527–634.

8. Clark, Samuel K.; and Dodge, Richard N.: *Heat Generation in Aircraft Tires Under Free Rolling Conditions.* NASA CR-3629, 1982.

9. Clark, Samuel K.; and Dodge, Richard N.: *Heat Generation in Aircraft Tires Under Braked Rolling Conditions*. NASA CR-3768, 1984.

10. McCarty, John Locke; and Tanner, John A.: *Temperature Distribution in an Aircraft Tire at Low Ground Speeds*. NASA TP-2195, 1983.

11. Schaeffer, Harry G.; and Ball, Robert E.: Nonlinear Deflections of Asymmetrically Loaded Shells of Revolution. AIAA-68-292, Apr. 1968.

12. Wunderlich, W.; Cramer, H.; and Obrecht, H.: Application of Ring Elements in the Nonlinear Analysis of Shells of Revolution Under Nonaxisymmetric Loading. *Comput. Methods Appl. Mech. & Eng.*, vol. 51, nos. 1–3, Sept. 1985, pp. 259–275.

13. Noor, Ahmed K.: On Making Large Nonlinear Problems Small. *Comput. Methods Appl. Mech. & Eng.*, vol. 34, nos. 1–3, Sept. 1982, pp. 955–985.

14. Noor, Ahmed K.; Andersen, Carl M.; and Tanner, John A.: *Mixed Models and Reduction Techniques for Large-Rotation, Nonlinear Analysis of Shells of Revolution With Application to Tires*. NASA TP-2343, 1984.

15. Noor, Ahmed K.: Reduction Method for the Non-Linear Analysis of Symmetric Anisotropic Panels. *Int. J. Numer. Methods Eng.*, vol. 23, 1986, pp. 1329–1341.

16. Noor, Ahmed K.; and Peters, Jeanne M.: Nonlinear Analysis of Anisotropic Panels. *AIAA J.*, vol. 24, no. 9, Sept. 1986, pp. 1545–1553.

17. Noor, Ahmed K.; Andersen, Carl M.; and Tanner, John A.: *Exploiting Symmetries in the Modeling and Analysis of Tires*. NASA TP-2649, 1987.

18. Noor, Ahmed K.; and Tanner, John A.: *Advances in Contact Algorithms and Their Application to Tires*. NASA TP-2781, 1988.

19. Sanders, J. Lyell, Jr.: Nonlinear Theories for Thin Shells. *Q. Appl. Math*., vol. 21, no. 1, Apr. 1963, pp. 21–36.

20. Budiansky, Bernard: Notes on Nonlinear Shell Theory. *J. Appl. Mech.*, vol. 35, no. 2, June 1968, pp. 393–401.

21. Simo, Juan C.; Wriggers, Peter; and Taylor, Robert L.: A Perturbed Lagrangian Formulation for the Finite Element Solution of Contact Problems. *Comput. Methods Appl. Mech. & Eng*., vol. 50, no. 2, Aug. 1985, pp. 163–180.

22. Stein, E.; Wagner, W.; and Wriggers, P.: Finite Element Postbuckling Analysis of Shells With Nonlinear Contact Constraints. *Finite Element Methods for Nonlinear Problems*, P. G. Bergan, K. J. Bathe, and W. Wunderlich, eds., Springer-Verlag, 1986, pp. 719–744.

23. Wriggers, Peter; and Nour-Omid, Bahram: *Solution Methods for Contact Problems.* Rep. No. UCB/SESM-84/09 (Contract N00014-76-C-0013), Dep. of Civil Engineering, Univ. of California, July 1984.

24. Concus, Paul; Golub, Gene H.; and O'Leary, Dianne P.: A Generalized Conjugate Gradient Method for the Numerical Solution of Elliptic Partial Differential Equations. *Sparse Matrix Computations*. James R. Bunch and Donald J. Rose, eds., Academic Press Inc., 1976, pp. 309–332.

25. Adams, Loyce: m-Step Preconditioned Conjugate Gradient Methods. *SIAM J. Sci. & Stat. Comput.*, vol. 6, no. 2, Apr. 1985, pp. 452–463.

26. Tanner, J. A.; Martinson, V. J.; and Robinson, M. P.: Static Frictional Contact of the Space Shuttle Nose-Gear Tire. *Tire Sci. & Tech.*, vol. 22, no. 4, Oct.–Dec. 1994.

27. Tanner, John A.: *Computational Methods for Frictional Contact With Applications to the Space Shuttle Orbiter Nose-Gear Tire—Comparisons of Experimental Measurements and Analytical Predictions*. NASA TP-3573, 1996.

28. Wriggers, P.; Wagner, W.; and Stein, E.: Algorithms for Non-Linear Contact Constraints With Application to Stability Problems of Rods and Shells. *Comput. Mech*., vol. 2, 1987, pp. 215–230.

29. Noor, Ahmed K.; and Kim, Kyun O.: Mixed Finite Element Formulation for Frictionless Contact Problems. *Finite Elem. Anal. & Design*, vol. 4, no. 4, 1989, pp. 315–332.

30. Torstenfelt, Bo: Finite Elements in Contact and Friction Applications. Linköping Studies in Science and Technology. Dissertations. No. 103, Div. of Solid Mechanics and Strength of

Materials, Dep. of Mechanical Engineering, Linköping Univ. (Linköping, Sweden), 1983.

31. Kim, Kyun O.; Noor, Ahmed K.; and Tanner, John A.: *Modeling and Analysis of the Space Shuttle Nose-Gear Tire With Semianalytic Finite Elements*. NASA TP-2977, 1990.

32. Kim, Kyun O.; Tanner, John A.; Noor, Ahmed K.; and Robinson, Martha P.: *Computational Methods for Frictionless Contact With Application to Space Shuttle Orbiter Nose-Gear Tires*. NASA TP-3073, 1991.

33. Smiley, Robert F.; and Horne, Walter B.: *Mechanical Properties of Pneumatic Tires With Special Reference to Modern Aircraft Tires*. NASA TR R-64, 1960. (Supersedes NACA TN 4110.)

34. Fröberg, Carl-Erik: *Introduction to Numerical Analysis*. Addison-Wesley Publ. Co., Inc., 1965.

Table 1. Characteristics of Mixed Finite-Element Models Used in Numerical Studies

Designation	Number of displacement nodes	Maximum number of Lagrange multipliers	Number of parameters per stress resultant	Number of quadrature points*
M9-4	3×3	3×3	2×2	3×3

*All elemental arrays are evaluated using Gauss-Legendre quadrature formulas except for $[Q]$, $[R]$, and $\{g_0\}$, which are evaluated using Newton-Cotes formulas.

Table 2. Effect of Relaxation Parameter on Convergence of Contact-Friction Algorithm

[ε_n = 1.0 E+12; ε_t = 1.5 E+06; μ_{static} = 0.6; $\mu_{dynamic}$ = 0.51]

Step	ε_{relax}	Normal deflection, in.	Normal load, lb	Iterations
1	1.0	0	0	6
2		.025	86.63	4
3		.05	221.43	(a)
4		.1	515.07	(a)
5		.2	1256.76	(a)
6		.3	2112.22	(a)
7		.33	2315.18	(a)
Total				10[a]
1	0.75	0	0	6
2		.025	86.63	4
3		.05	221.43	28[b]
4		.1	515.07	15[b]
5		.2	1256.76	22[b]
6		.3	2112.22	25[b]
7		.33	2315.18	26[b]
Total				126[b]
1	0.5	0	0	6
2		.025	86.63	4
3		.05	221.43	4
4		.1	515.07	3
5		.2	1256.76	7
6		.3	2112.22	8
7		.33	2315.18	4
Total				36
1	0.25	0	0	6
2		.025	86.63	4
3		.05	221.43	32
4		.1	515.07	20
5		.2	1256.76	27
6		.3	2112.22	28
7		.33	2315.18	32
Total				149

[a]Did not converge in 40 iterations.
[b]Oscillating friction forces.

Table 3. Iteration History for Contact Node 36 Illustrating Oscillating Friction-Load Intensities

[ε_{relax} = 0.75; ε_n = 1.0 E+12; ε_t = 1.5 E+06; μ_{static} = 0.6; $\mu_{dynamic}$ = 0.51; Normal deflection = 0.05 in.]

Iteration	Contact flag	λ_w, psi	λ_u, psi	λ_v, psi	Lateral friction slip energy, in-lb	Drag friction slip energy, in-lb
1	1	0.0000 E+00	0.0000 E+00	0.0000 E+00	0.0000 E+00	0.0000 E+00
2	2	.1238 E+01	.6313 E+00	.2232 E–01	–.7834 E–04	–.9799 E–07
3	1	.1412 E+01	.6313 E+00	.2232 E–01	.0000 E+00	.0000 E+00
4	2	.1413 E+01	–.7206 E+00	–.2548 E–01	–.4470 E–04	–.5591 E–07
5	1	.1326 E+01	–.7206 E+00	–.2548 E–01	.0000 E+00	.0000 E+00
6	2	.1326 E+01	.6759 E+00	.2390 E–01	–.2096 E–04	–.2622 E–07
7	1	.1370 E+01	.6759 E+00	.2390 E–01	.0000 E+00	.0000 E+00
8	2	.1370 E+01	–.6982 E+00	–.2469 E–01	–.1082 E–04	–.1354 E–07
9	1	.1348 E+01	–.6982 E+00	–.2469 E–01	.0000 E+00	.0000 E+00
10	2	.1348 E+01	.6871 E+00	.2430 E–01	–.5327 E–05	–.6663 E–08
11	1	.1359 E+01	.6871 E+00	.2430 E–01	.0000 E+00	.0000 E+00
12	2	.1359 E+01	–.6927 E+00	–.2449 E–01	–.2685 E–05	–.3359 E–08
13	1	.1353 E+01	–.6927 E+00	–.2449 E–01	.0000 E+00	.0000 E+00
14	2	.1353 E+01	.6899 E+00	.2439 E–01	–.1337 E–05	–.1672 E–08
15	1	.1356 E+01	.6899 E+00	.2439 E–01	.0000 E+00	.0000 E+00
16	2	.1356 E+01	–.6913 E+00	–.2444 E–01	–.6700 E–06	–.8380 E–09
17	1	.1354 E+01	–.6913 E+00	–.2444 E–01	.0000 E+00	.0000 E+00
18	2	.1354 E+01	.6902 E+00	.2441 E–01	–.3345 E–06	–.4183 E–09
19	1	.1355 E+01	.6902 E+00	.2441 E–01	.0000 E+00	.0000 E+00
20	2	.1355 E+01	–.6907 E+00	–.2442 E–01	–.1673 E–06	.0000 E+00
21	1	.1354 E+01	–.6907 E+00	–.2442 E–01	.0000 E+00	.0000 E+00
22	2	.1354 E+01	.6905 E+00	.2442 E–01	–.8365 E–07	.0000 E+00
23	1	.1355 E+01	.6905 E+00	.2442 E–01	.0000 E+00	.0000 E+00
24	2	.1355 E+01	–.6906 E+00	–.2442 E–01	–.4183 E–07	.0000 E+00
25	1	.1354 E+01	–.6906 E+00	–.2442 E–01	.0000 E+00	.0000 E+00
26	2	.1354 E+01	.6905 E+00	.2442 E–01	–.2091 E–07	.0000 E+00
27	1	.1354 E+01	.6905 E+00	.2442 E–01	.0000 E+00	.0000 E+00
28	1	.1354 E+01	–.4183 E+00	–.1479 E–01	.0000 E+00	.0000 E+00
Total					–.1655 E–03	–.2066 E–06

Table 4. Effect of Tangential Penalty Parameter on Convergence of Contact-Friction Algorithm

[ε_{relax} = 0.5; ε_n = 1.0 E+12; μ_{static} = 0.6; $\mu_{dynamic}$ = 0.51]

Step	ε_t	Normal deflection, in.	Normal load, lb	Iterations
1	1.0	0	0	6
2		.025	86.63	4
3		.05	221.43	3
4		.1	515.07	3
5		.2	1256.76	7
6		.3	2112.22	5
7		.33	2315.18	3
Total				31
1	1.5 E+03	0	0	6
2		.025	86.63	4
3		.05	221.43	4
4		.1	515.07	3
5		.2	1256.76	7
6		.3	2112.22	5
7		.33	2315.18	5
Total				34
1	1.5 E+06	0	0	6
2		.025	86.63	4
3		.05	221.43	4
4		.1	515.07	3
5		.2	1256.76	7
6		.3	2112.22	8
7		.33	2315.18	4
Total				36
1	1.0 E+12	0	0	6
2		.025	86.63	6
3		.05	221.43	6
4		.1	515.07	5
5		.2	1256.76	7
6		.3	2112.22	7
7		.33	2315.18	8
Total				45

Table 5. Effect of Static and Dynamic Friction Coefficients on Convergence of Contact-Friction Algorithm

[ε_{relax} = 0.5; ε_n = 1.0 E+12; ε_t = 1.5 E+03]

Step	Friction coefficient	Normal deflection, in.	Normal load, lb	Iterations
1	μ_{static} = 0.3	0	0	6
2	$\mu_{dynamic}$ = 0.26	.025	86.63	7
3		.05	221.43	7
4		.1	515.07	5
5		.2	1256.76	8
6		.3	2112.22	8
7		.33	2315.18	4
Total				45
1	μ_{static} = 0.6	0	0	6
2	$\mu_{dynamic}$ = 0.51	.025	86.63	4
3		.05	221.43	4
4		.1	515.07	3
5		.2	1256.76	7
6		.3	2112.22	5
7		.33	2315.18	5
Total				34
1	μ_{static} = 1.0	0	0	6
2	$\mu_{dynamic}$ = 0.85	.025	86.63	6
3		.05	221.43	7
4		.1	515.07	5
5		.2	1256.76	8
6		.3	2112.22	8
7		.33	2315.18	4
Total				44

Table 6. Effect of Load Step Size on Convergence of Contact-Friction Algorithm

[ε_{relax} = 0.5; ε_t = 1.5 E+03; ε_n = 1.0 E+12; μ_{static} = 0.6; $\mu_{dynamic}$ = 0.51]

Step	Normal deflection, in.	Normal load, lb	Iterations
1	0	0	6
2	.025	86.63	4
3	.05	221.43	4
4	.1	515.07	3
5	.2	1256.76	7
6	.3	2112.22	5
7	.33	2315.18	5
8	.4	2806.26	4
9	.5	3435.70	8
10	.6	3998.32	6
Total			52
1	0	0	6
2	.025	86.63	4
3	.2	1255.77	8
4	.4	2779.85	5
5	.6	3974.51	5
Total			28
1	0	0	6
2	.025	86.63	4
3	.3	2110.36	7
4	.6	3962.25	9
Total			26

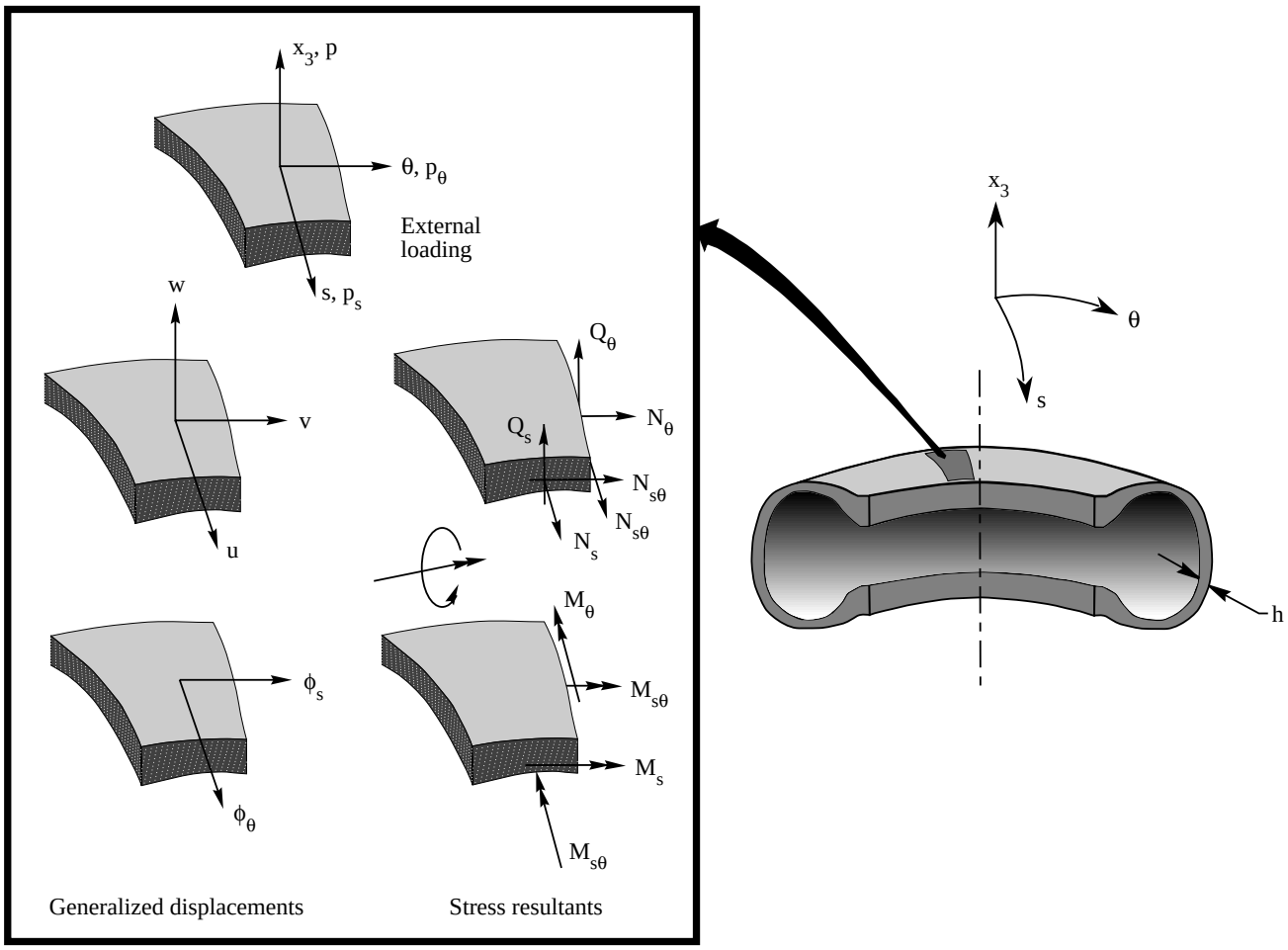

(a) External loading, generalized displacements, and stress resultants.

Figure 1. Two-dimensional model of tire and sign convention.

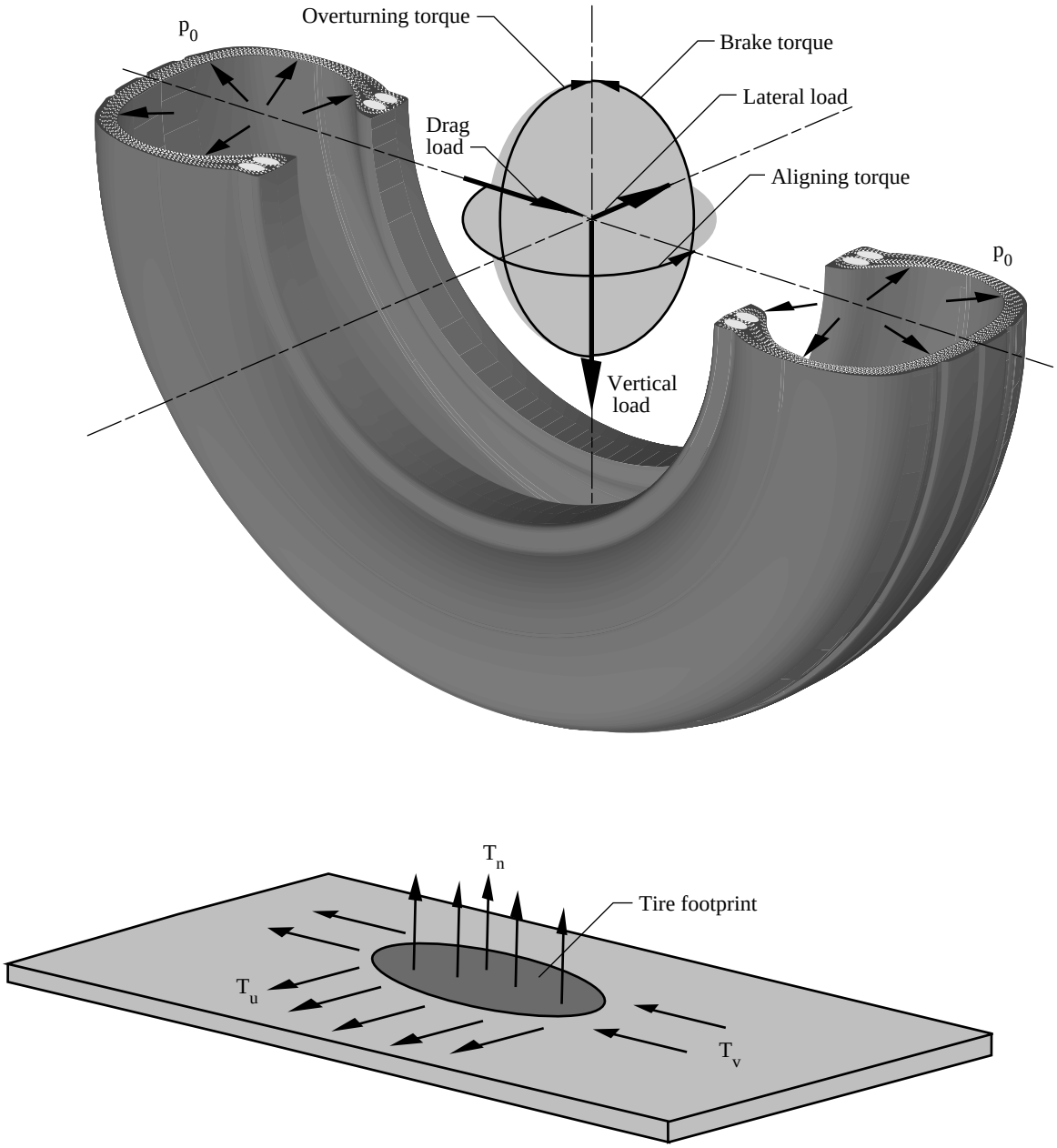

(b) Free body diagram of applied loads, torques, and contact forces.

Figure 1. Concluded.

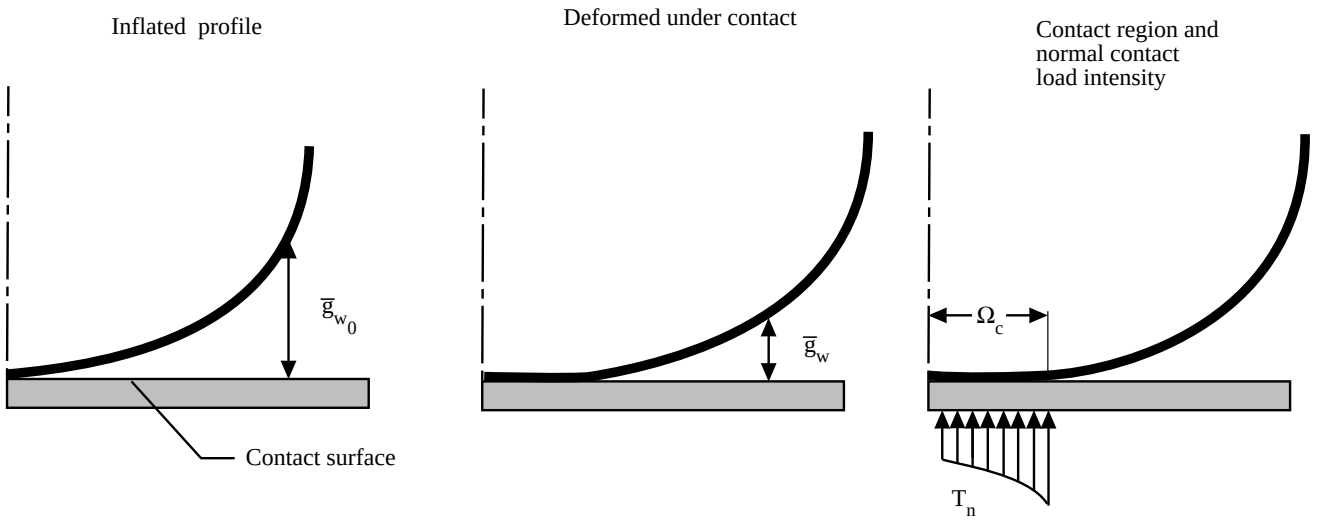

(a) Normal gaps.

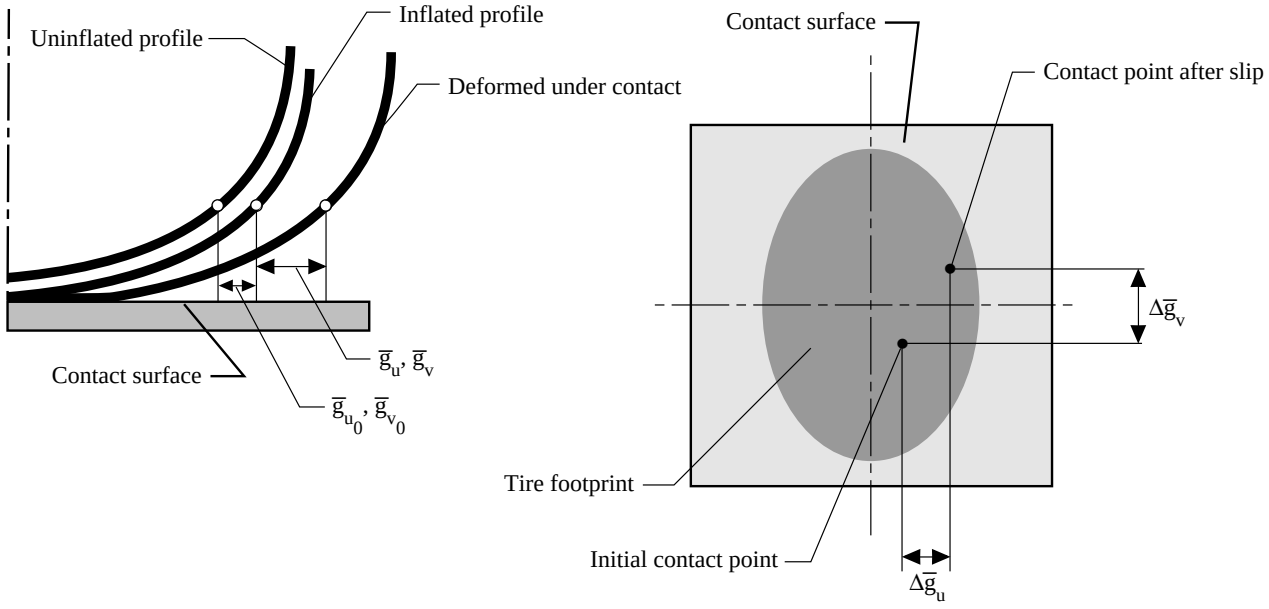

(b) Transverse gaps.

Figure 2. Schematic representation of gap terms associated with tire contact problems.

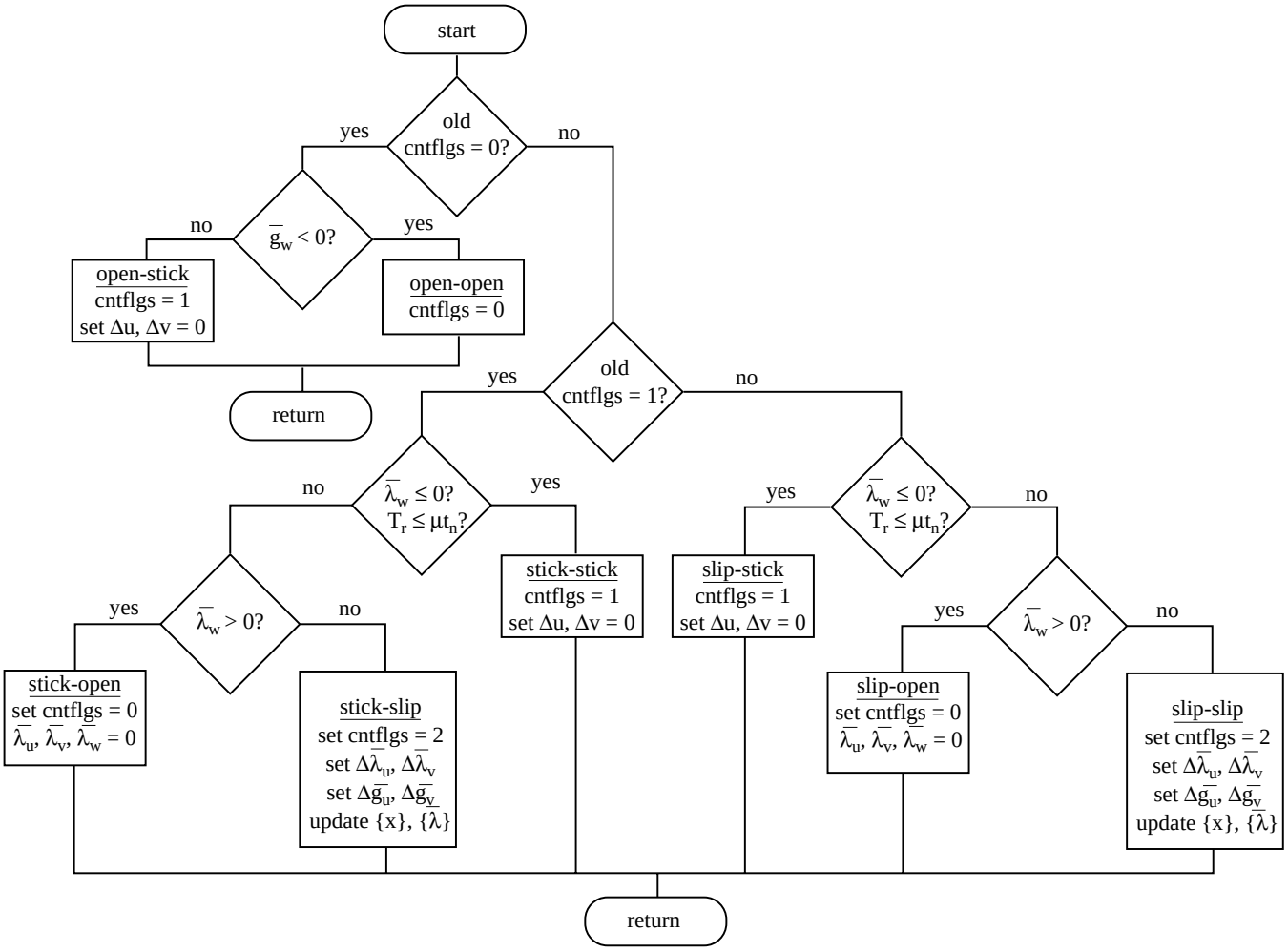

Figure 3. Schematic diagram of contact-friction algorithm logic.

- Finite element:

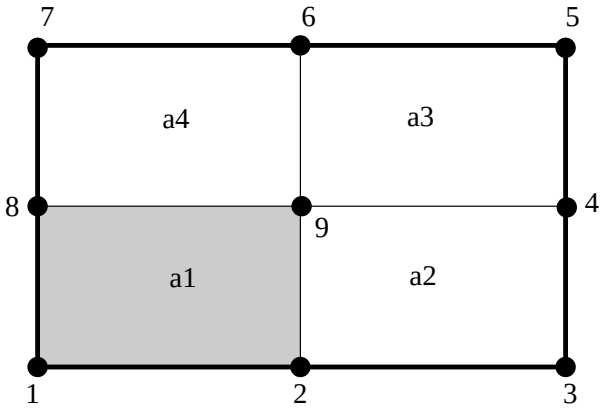

- Typical quadrant:

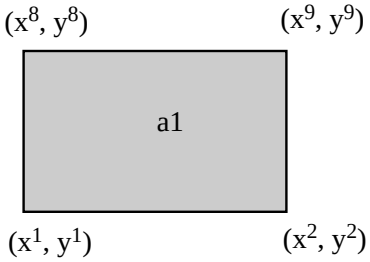

- Typical quadrant area:

$$A^1_{quad} = 0.5*(x^1y^2 - x^2y^1 + x^2y^9 - x^9y^2 + x^9y^1 - x^1y^9 + x^1y^9 - x^9y^1 + x^9y^8 - x^8y^9 + x^8y^1 - x^1y^8)$$

- Nodal areas:

$$A^1_{node} = 0.25*A^1_{quad}$$
$$A^2_{node} = 0.25*(A^1_{quad} + A^2_{quad})$$
$$A^3_{node} = 0.25*A^2_{quad}$$
$$A^4_{node} = 0.25*(A^2_{quad} + A^3_{quad})$$
$$A^5_{node} = 0.25*A^3_{quad}$$
$$A^6_{node} = 0.25*(A^3_{quad} + A^4_{quad})$$
$$A^7_{node} = 0.25*A^4_{quad}$$
$$A^8_{node} = 0.25*(A^4_{quad} + A^1_{quad})$$
$$A^9_{node} = 0.25*(A^1_{quad} + A^2_{quad} + A^3_{quad} + A^4_{quad})$$

Figure 4. Major characteristics of contact surface area algorithm.

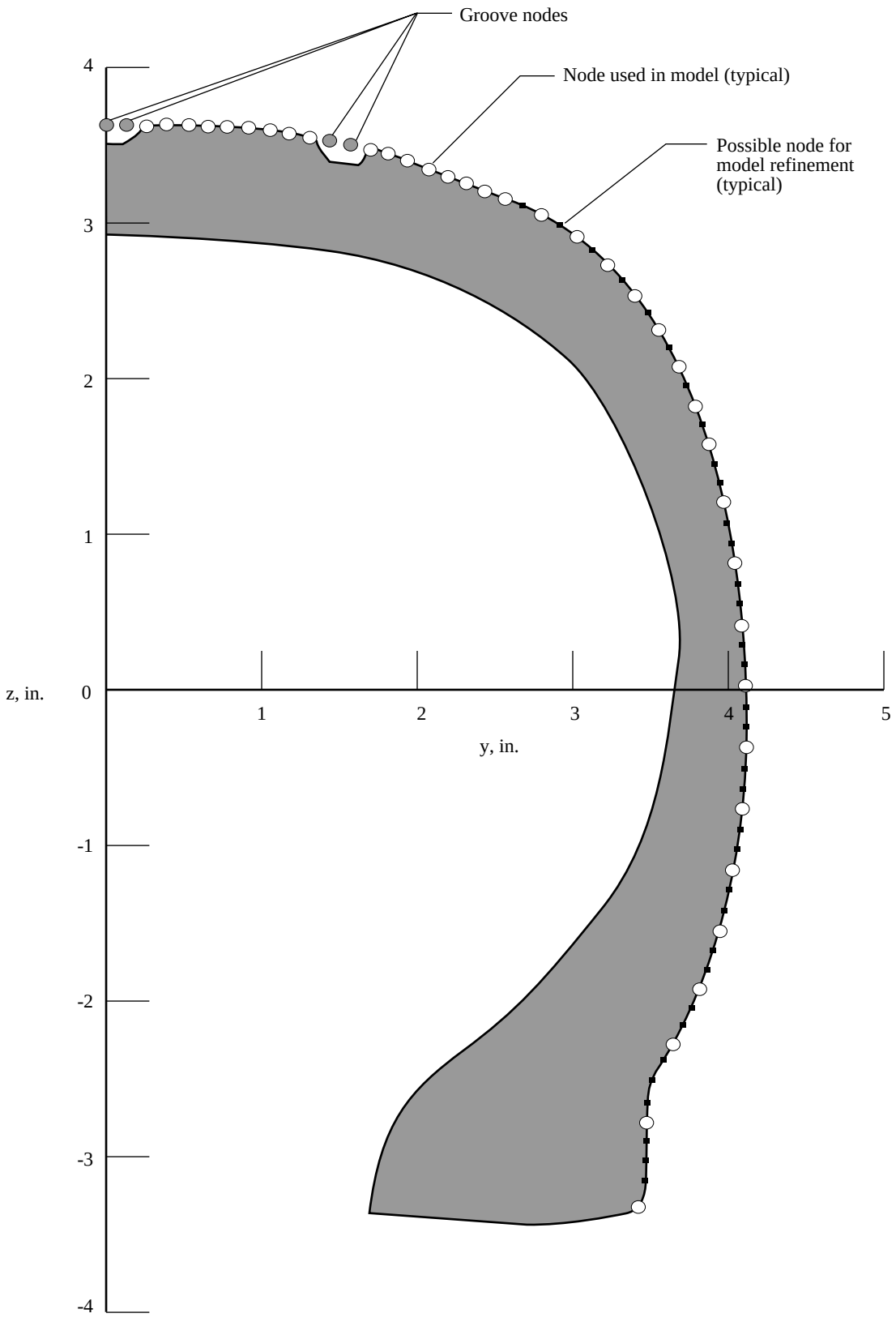

Figure 5. Meridional profile of Space Shuttle nose-gear tire models denoting node point locations.

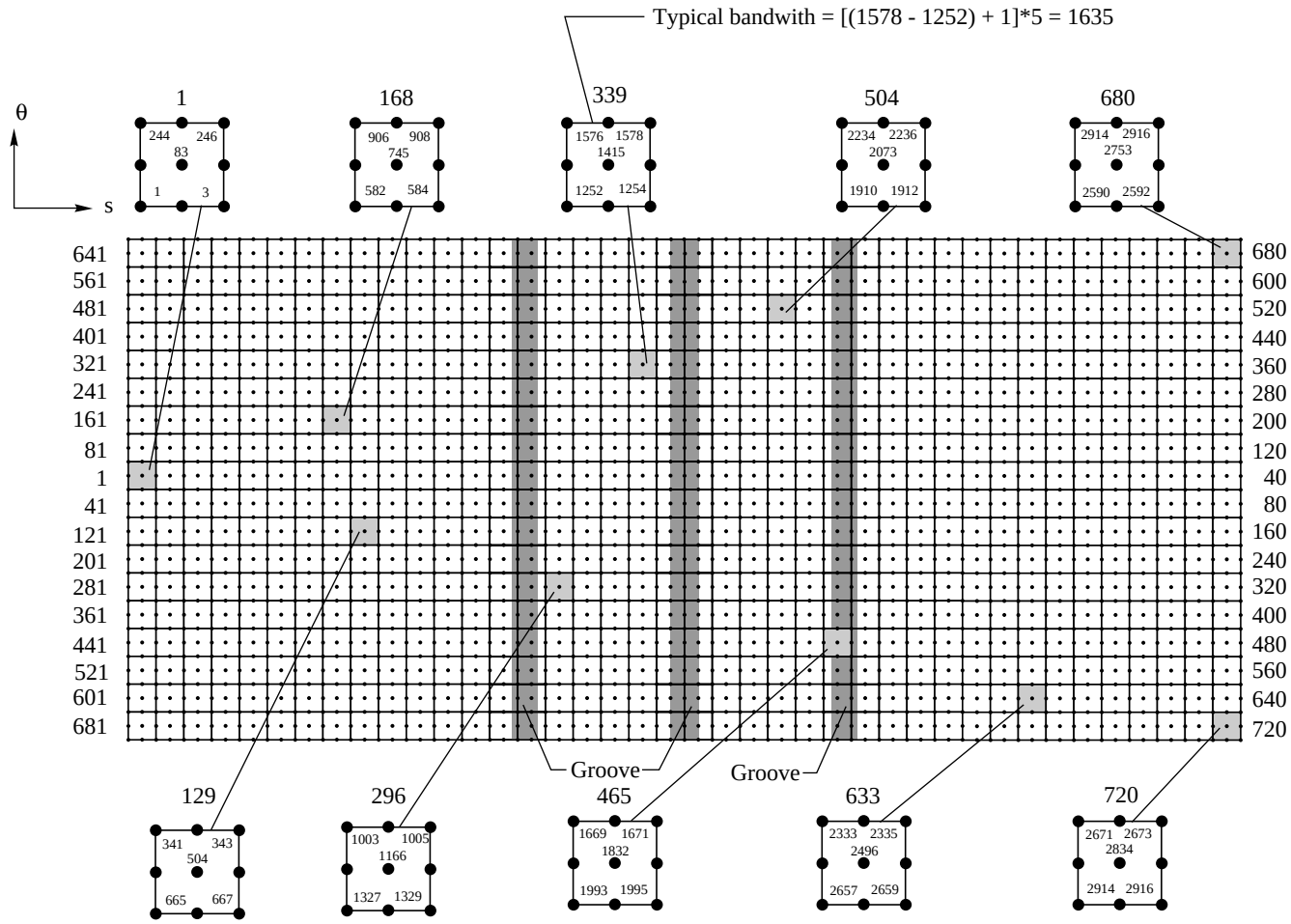

Figure 6. Typical array of finite elements and nodes used to model the Space Shuttle nose-gear tire.

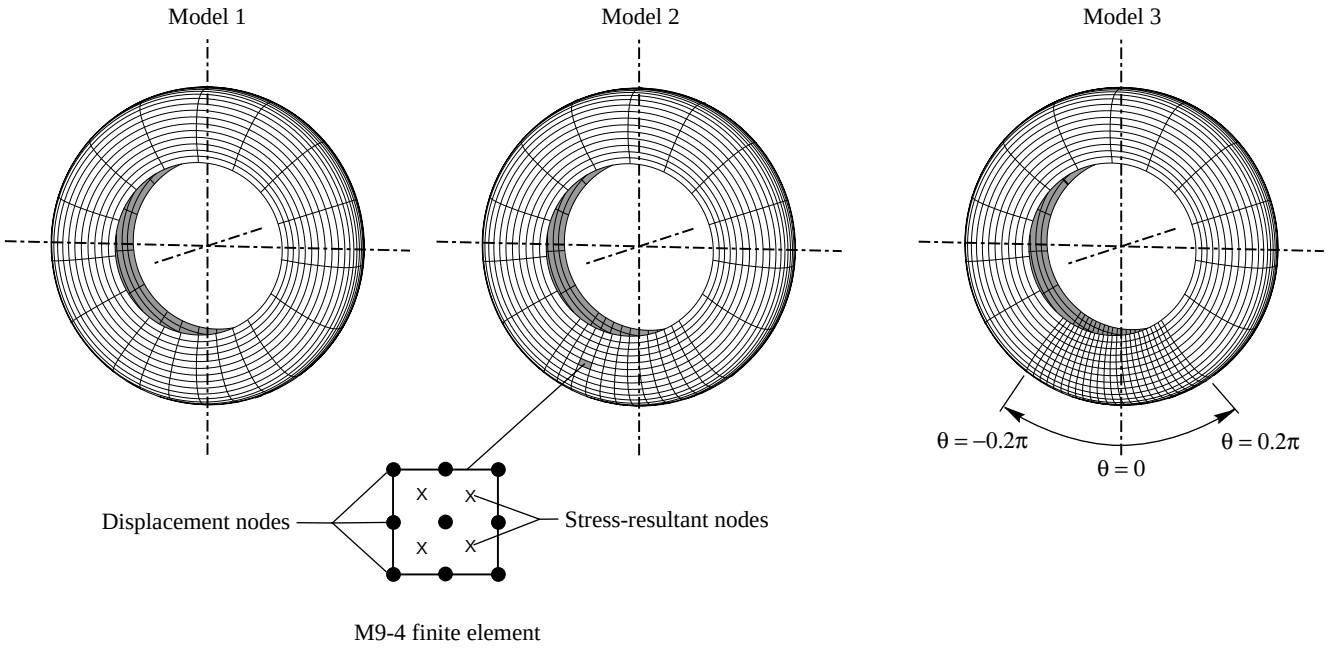

Sector	Number of elements (M9-4) for—		
	Model 1	Model 2	Model 3
$-0.2\pi \le \theta \le 0.2\pi$	240 (40 × 6)	480 (40 × 12)	960 (40 × 24)
$\theta < -0.2\pi, \theta > 0.2\pi$	480 (40 × 12)	480 (40 × 12)	480 (40 × 12)
Total	720 (40 × 18)	960 (30 × 24)	1440 (40 × 36)

Figure 7. Finite-element models of Space Shuttle nose-gear tire used in present study.

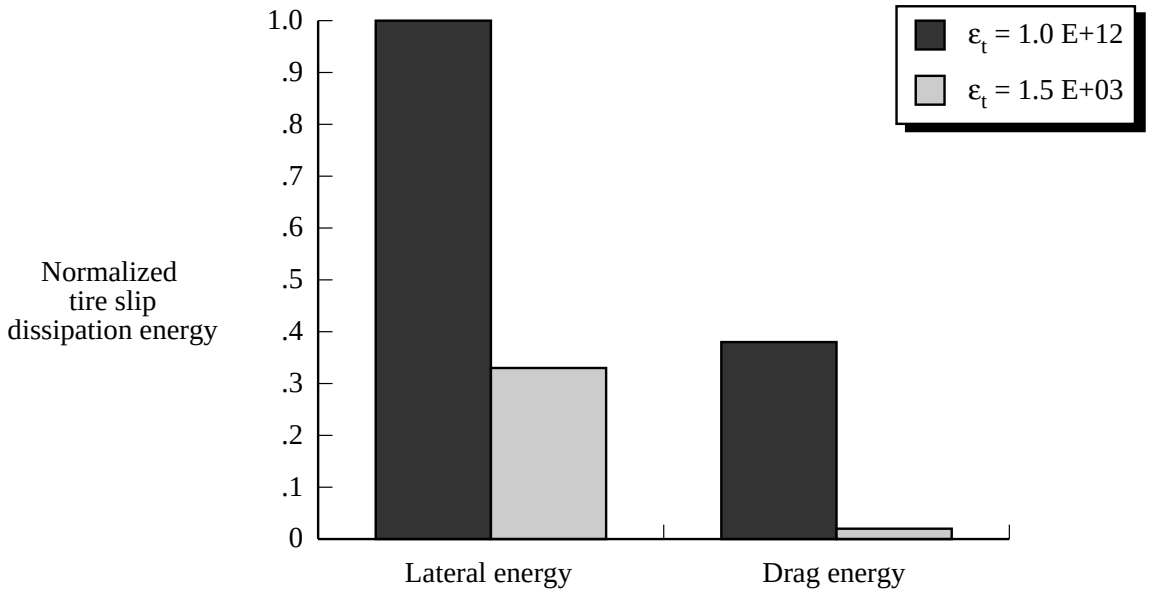

Figure 8. Effect of tangential penalty parameter variation on slip energy dissipated by tire. $\varepsilon_{relax} = 0.5$; $\varepsilon_n = 1.0$ E+12; $\mu_{static} = 0.6$; $\mu_{dynamic} = 0.51$; normal deflection = 0.3 in.

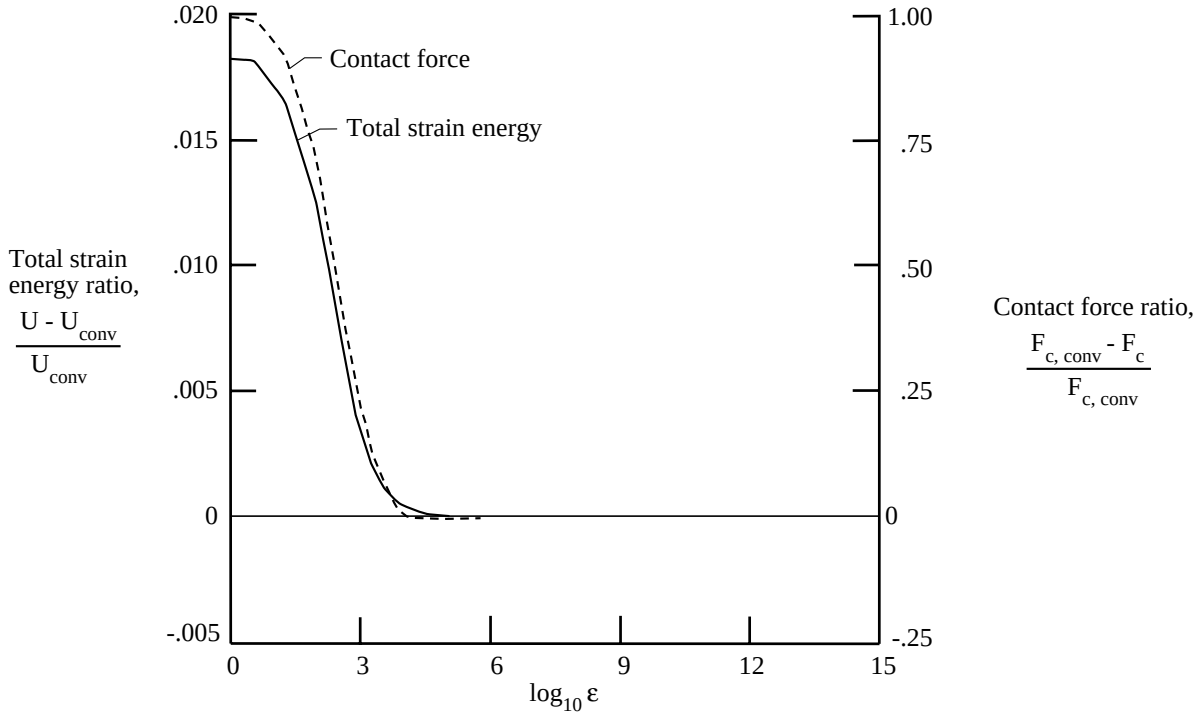

Figure 9. Effect of magnitude of normal penalty parameter ε_n on accuracy of total strain energy and contact force. $p_0 = 300$ psi.

REPORT DOCUMENTATION PAGE

Form Approved
OMB No. 0704-0188

1. AGENCY USE ONLY *(Leave blank)*	2. REPORT DATE	3. REPORT TYPE AND DATES COVERED
	April 1996	Technical Paper

4. TITLE AND SUBTITLE
Computational Methods for Frictional Contact With Applications to the Space Shuttle Orbiter Nose-Gear Tire
Development of Frictional Contact Algorithm

5. FUNDING NUMBERS
WU 505-63-50-19

6. AUTHOR(S)
John A. Tanner

7. PERFORMING ORGANIZATION NAME(S) AND ADDRESS(ES)
NASA Langley Research Center
Hampton, VA 23681-0001

8. PERFORMING ORGANIZATION REPORT NUMBER
L-17211B

9. SPONSORING/MONITORING AGENCY NAME(S) AND ADDRESS(ES)
National Aeronautics and Space Administration
Washington, DC 20546-0001

10. SPONSORING/MONITORING AGENCY REPORT NUMBER
NASA TP-3574

11. SUPPLEMENTARY NOTES

12a. DISTRIBUTION/AVAILABILITY STATEMENT
Unclassified–Unlimited
Subject Category 39
Availability: NASA CASI (301) 621-0390

12b. DISTRIBUTION CODE

13. ABSTRACT *(Maximum 200 words)*

A computational procedure is presented for the solution of frictional contact problems for aircraft tires. A Space Shuttle nose-gear tire is modeled using a two-dimensional laminated anisotropic shell theory which includes the effects of variations in material and geometric parameters, transverse-shear deformation, and geometric nonlinearities. Contact conditions are incorporated into the formulation by using a perturbed Lagrangian approach with the fundamental unknowns consisting of the stress resultants, the generalized displacements, and the Lagrange multipliers associated with both contact and friction conditions. The contact-friction algorithm is based on a modified Coulomb friction law. A modified two-field, mixed-variational principle is used to obtain elemental arrays. This modification consists of augmenting the functional of that principle by two terms: the Lagrange multiplier vector associated with normal and tangential node contact-load intensities and a regularization term that is quadratic in the Lagrange multiplier vector. These capabilities and computational features are incorporated into an in-house computer code. Experimental measurements were taken to define the response of the Space Shuttle nose-gear tire to inflation-pressure loads and to inflation-pressure loads combined with normal static loads against a rigid flat plate. These experimental results describe the meridional growth of the tire cross section caused by inflation loading, the static load-deflection characteristics of the tire, the geometry of the tire footprint under static loading conditions, and the normal and tangential load-intensity distributions in the tire footprint for the various static vertical loading conditions. Numerical results were obtained for the Space Shuttle nose-gear tire subjected to inflation pressure loads and combined inflation pressure and contact loads against a rigid flat plate. The experimental measurements and the numerical results are compared.

14. SUBJECT TERMS
Finite elements; Tire modeling; Frictional contact; Shuttle; Nose-gear; Shell theory

15. NUMBER OF PAGES
48

16. PRICE CODE
A03

17. SECURITY CLASSIFICATION OF REPORT	18. SECURITY CLASSIFICATION OF THIS PAGE	19. SECURITY CLASSIFICATION OF ABSTRACT	20. LIMITATION OF ABSTRACT
Unclassified	Unclassified	Unclassified	